PETRONAS-Imperial Centre for Engineering of Multiphase Systems

Carbonate Rock Failure and Solids Production: *Onset, Rate, and Volume Predictions*

Ado Farsi, John-Paul Latham, and Robert W. Zimmerman

Department of Earth Science and Engineering
Imperial College
London, UK

March 2022 Final Report

Executive Summary

This final report covers work done during the project "Carbonate Rock Failure and Solids Production". The goal of the project is to develop tools to predict and/or mitigate the problem of solids production in carbonate reservoirs. To this end, novel laboratory experiments have been conducted on solids production in thick-walled cylinders, under realistic stress and flowrate conditions, using cores provided by Petronas. The experiments are being modelled with an in-house Finite-Discrete Element (FDEM) code.

This report is structured in four main sections as follows. In the first main section, the theoretical background, and governing equations for simulating stress and fragmentation behaviour of circular boreholes in poroelastic rocks, including fluid flow effects, are discussed. After an introduction on hydromechanical coupling with rock mechanics applications, the solution is presented for the problem of radial fluid flow in a thick-walled cylinder. In the next section, the governing equations for modelling stress and deformation in a poroelastic material are introduced. Consequently, the main computational implementations that are employed to solve the previously introduced governing equations in a combined finite-discrete element framework are described. In the next section, three numerical examples of wells in a poroelastic medium are introduced, and the results are compared with the solutions of the governing equation obtained from Firedrake, a python-based software for the solution of partial differential equations. In the last section dealing with theoretical background, the key results of the proposed method are highlighted, and the conclusions are summarised. The next main section presents the results of the thick-walled cylinder tests, and their interpretation for the mechanical characterisation and solids production estimations from wells in carbonate reservoirs. The final main section contains the preliminary validation of the FDEM workflow for the estimation of solids production onset and rate.

Table of contents

Introduction

Oil wells can suffer from the dislodging of solid particles, leading to a flow of solids up the wellbore. This occurrence, known as "solids production", has detrimental economic and safety consequences. Additionally, there are additional costs associated with handling solids at the wellhead. Solids production in certain wells can be so severe that the borehole will be blocked and the well will need to be abandoned.

Sand reservoirs are largely affected by solid production, where individual grains of sand are released from the reservoir rock at the borehole walls and/or perforations, giving rise to the term *sand production* or *sanding*. Consequently, there is a considerable literature and body of knowledge related to the production of solids from sand reservoirs.

However, solids production can also occur in carbonate deposits. PETRONAS has encountered such problems in several wells. Due to the relatively poor understanding of the problem of solids production from carbonate reservoirs, PETRONAS has proposed to undertake a research program to study this phenomenon with the aim of providing tools to predict and/or mitigate this problem.

With the aim of defining and validating a model for the prediction of carbonate solid production, the computational approach for an efficient Finite-Discrete Element (FDEM) workflow for the simulation of circular boreholes in poroelastic media is described and validated in this report. This document also contains some of the experimental results for the mechanical characterisation and for the validation of the numerical prediction. In addition, this document contains the preliminary FDEM simulations of Thick Wall Cylinder (TWC) tests that have been conducted, including the effects of pore pressure and fluid forces. At this stage of the project, the full set of mechanical properties of the tested TWC samples has not yet been made available for model calibration. For this reason, the model parameters in the simulation were based on the mechanical properties that were obtained from previous characterisations of carbonate rock samples presented by PETRONAS. The report shows a good agreement between simulations and experiments, both in terms of onset of solids production and cumulative solids produced.

Report Summary

In Report 1, we provide two main sections. The first section is a brief review of the key literature relating to the solids production processes in sandstones, and to the extent possible highlighting any literature on the carbonate reservoir rocks from the Central Luconia platform region in the offshore waters of Sarawak, Eastern Malaysia, or South-East Asia, with an emphasis on any literature suggesting similarities or differences to be expected between weak carbonate and weak sandstone solids production. The second section is a description of the FDEM modelling technology to be used for the simulation of solids production, including the progress to date in setting up the FDEM model, verification through benchmark deformation problems, and an illustration of the expression of borehole wall collapse with production of solid fragments. Finally, conclusions are drawn, and the next steps indicated.

Constitutive models are powerful and widely used in continuum mechanics and computational mechanics to simulate continuum behaviour, including dissipative visco-plastic yielding with varying degrees of sophistication for rate dependence, hardening, softening, dilatancy, compaction, *etc*. The key novelty in this project is to introduce a fresh approach that exploits discontinuum mechanics, namely FDEM modelling, for which the concept of a constitutive model is largely replaced. The yielding behaviour of the modelled rock is an emergent phenomenon that is controlled by properties assigned to joint elements that can open in tension and shear in accordance with fundamental fracture mechanics and frictional cohesive material principles. As confining stresses increase, the irrecoverable deformation is expressed by increasingly densely spaced local shears, as can often be observed in the micro-structure of rocks yielding at the higher confinements that are found in reservoirs to a few kilometres depth. Given that fragments of rock are created in the wall-rock deformation process, *i.e.* solids production occurs in the FDEM modelling, there is the potential for a more direct evaluation of solids production rate than can be achieved with continuum plasticity models.

1 Literature review on solids production

1.1 Introduction

The objective of this ICL/Petronas project is to apply the FDEM numerical modelling approach to borehole wall rock failure, and thereby improve our understanding of progressive borehole instability and solids production processes that will enable reservoir engineers to exploit open-hole gas extraction at such great depths. Borehole wall stability analysis begins with a simple analysis of stress around a circular opening using the Kirsch equations. After the Petronas team provided ICL with a brief introduction to the weak carbonate rock properties (UCS of perhaps as low as 5 to 15 MPa) in the Luconia platform reservoirs of interest, together with data suggesting the bounds of *in-situ* stress and pore pressure likely to be encountered at the productive well depths in question, and following the assumptions of the simple theory, it was concluded that the walls of the open holes would be expected to collapse by classical shear failure breakouts at these depths. However, in practice, the boreholes can be made to operate at considerable depths without encountering solids production problems. A literature review has been conducted specifically to better understand the current theories and methodologies used to test rock specimens, and to use well-log data and numerically model and manage solids production in the Luconia platform carbonate reservoirs.

1.1 The role of TWC testing in solids production prediction

A range of mechanisms potentially responsible for 'sanding failure', including compressive, tensile, and erosional mechanisms, were critically reviewed by Veeken *et al.* (Veeken et al., 1991). Criteria based on borehole wall tangential stresses exceeding the shear strengths were considered to lead to highly variable predictions of shear failure, depending on the constitutive model used, and were also found to be too conservative - *i.e.*, the onset of sanding in field conditions occurs at higher stresses than predicted. Thick-wall cylinder (TWC), hollow cylinder (HC), or hollow prism (HP) specimen tests, with no pressures applied within the hole and hydrostatically loaded to failure, have proved to be a successful strategy to better predict the strengthening effect occurring in borehole wall rock, as compared with uniaxial or triaxial rock strength data predictions. Wu and Tan (Wu & Tan, 2000) examined the relation between UCS and TWC collapse strengths in sandstones, showing that the TWC/UCS ratio increased nonlinearly as UCS values fell below 30 MPa, thereby deriving a useful empirical predictor of this ratio. The very weak rocks have high porosity, but non-linear elasticity was found to be relatively insignificant. The weaker rocks also deform more plastically, with higher residual strength to peak strength ratios at the same confinement, than do stronger, more brittle rocks. This fact prompted Wu and Tan to examine the microstructure of sandstones yielding by shear failure in both uniaxial solid cylinders, and TWC specimens which represent different loading and yielding stress paths in the wall rock, and to speculate whether failure was more localised or distributed pervasively in the different settings and whether grains were more or less constrained from rotation.

There is an extensive literature on sand production prediction models, such as reviewed by Rahmati *et al.* (Rahmati et al., 2013). Their review covers weak poorly consolidated and stronger sedimentary rock, hence coupled fluid and solid mechanics where flow velocity contributes to seepage drag forces and mobilisation of grains is included. Continuum plasticity numerical models, *i.e.,* with bifurcation solutions for shear initiation, were reported to encounter problems of mesh size, and a need for regularisation or refinement methods to model the individual shear bands using FEM. Discrete element methods applied to shear failure breakdown and sanding were in their relative infancy and flagged up as promising for hybrid approaches at the time of that review, which concluded that modelling tools are still unable to predict the sand mass and the rate of sanding in a reliable way. More recent numerical models are discussed further below.

Perhaps the most relevant research on theoretical approaches to understand the stability of borehole walls and conditions leading to sanding phenomena that are based on compressive failure theory can be found in the work of Papamichos and co-workers, (Papamichos, 2020; Papamichos et al., 2010, 2012). Papamichos and co-workers (Papamichos, 2020) show how some constitutive models other than Mohr-Coulomb, those which under higher confinements show an intermediate stress dependency of the yielding rock, lead to different predictions for development of stress anisotropy, and hence yielding behaviour. The stress changes cannot be predicted from purely poroelastic analysis. The dilatant or compacting yielding behaviour must follow the stress history. It is generally considered quite complex to derive the post-peak behaviour, and in (Papamichos, 2020), this complexity invites failure prediction based on calibration from experimental results. The most pragmatic methodology combines direct experimental data based on (advanced) TWC test results *e.g.* for critical strains, to overcome the complexity of computing the inelastic response - see the work by Younessi *et al.* (Younessi et al., 2018), discussed below - of the highly variable loading and pressure conditions possible in reservoirs.

In (Papamichos, 2020) and several other papers, 3D stress analysis is used to capture fully the axial compression effects on the local stress anisotropy for TWC tests. A typical vertical borehole in a normal faulting regime undergoes important stress changes during the depletion history and pressure drawdown applications. For example, due to the Poisson effect and poroelastic consequences of depleting pore pressure, while the vertical effective stress remains relatively unchanged, the horizontal effective stresses are increasing, according to the A-factor, sometimes referred to as the depletion constant (Zoback, 2007), thereby changing the stress anisotropy across the hole's diameter for horizontal holes or perforations in the normal faulting regime. Furthermore, as bottomhole pressures are reduced with increasing drawdown and depleting reservoir pressures, the confining pressure on the borehole wall provided by the bottom hole fluid pressure (which acts to resist shear failure driven by the maximum tangential compressive hoop stresses) is reduced. In addition, the local *in situ* stress is very dependent on the reservoir’s tectonic setting and hole orientation. The prediction model must be capable of assessing all such settings. In most theoretical analyses presented previously, significant poroelastic effects are often found to be expected, owing to the high porosities of these rocks and the large reservoir pore pressure differences that occur during depletion under different stages of reservoir development.

A full numerical model of shear failure and sand production initiation, taking account poroelasticity and inelastic yield behaviour, derived and validated for carbonate reservoir rocks, has yet to be presented in the literature. However, given that the UCS, Young's modulus, and porosity values provided by Petronas for carbonates from field F6 are in a similar range to the North Sea chalk reservoir analogues reported in Papamichos *et al.* (2012), there may be useful lessons to learn from research on constitutive models and borehole stability analyses of chalk rocks in North Sea reservoirs; see also Section 1.4. In this context it is also worth commenting that two different modes of failure of the chalk with brine TWC tests were noted, depending on the regime of pore pressure drawdown. The breakout failure and plastic shear strain observed for the depletion-type regime was considered similar to that observed in sandstone reservoir rocks. A so-called liquefaction type failure was observed for a drawdown type regime, which Papamichos *et al.* (2012) did not comment on further in relation to sandstones.

Khaksar *et al.* (Khaksar et al., 2008) presented a workflow and case history of sand production analysis in the Malaysian basin with horizontal wells, in oil bearing sandstones, but not in carbonates. They used both a 3D analysis based on TWC test results, and a 2D elasto-plastic model for failure zone growth. The depletion histories and drawdown scenarios in relation to a set of different TWC strengths were discussed. The analysis was conducted for relatively strong sandstones, with TWC > 24 MPa and low *in-situ* stress anisotropy, leading to the conclusion that there is no risk of sand production in the reservoir, although likely problems in the weaker shale horizons were identified.

Younessi et al. (Younessi et al., 2018) outlined two prediction methods. The analytical method is based on a poroelastic model with TWC rock strengths inferred from reservoir logs and an empirical effective rock strength factor (ESF), a multiplier usually between 2 and 3, that needs to be calibrated from sand production initiation data from the field. The numerical methodology for sanding onset prediction and control uses a continuum plasticity FEM model based on a constitutive model defined by triaxial core tests. The critical strain limit (CSL) for failure of the inner wall of the thick-walled cylinder is set as the criterion for rock failure and the onset of sand production. The analytical method based on default non-calibrated ESF was less reliable at sanding prediction than the core-based CSL defined by the numerical method. A combined analytical numerical (CAN) methodology and workflow with validation steps was carefully set out, and offers a promising framework for combining results with advanced TWC experiments, eventually providing a tool to model perforation or open hole effects under different far-field and drawdown pressures.

Experimental investigations of sanding at cylindrical perforations in the Red Wildmoor Sandstone (Tronvoll & Fjær, 1994) were some of the first detailed studies of perforation hole cavities with and without fluid flows driven from outside towards the inside of the cavity. This work showed that the evolution of the cavity failure (but not the initiation) was significantly affected by the seepage flows. Cuss *et al.* (Cuss et al., 2003) provided detailed analyses of the microstructural behaviour during breakout enlargement under hydrostatic compaction for three sandstone types, in scaled small 6 mm diameter bores traversing 60% of the length of the 25 mm diameter cylinders. They included an insightful discussion of pore collapse and significant inelastic strain before failure (not unrelated to the CSL mentioned above) in the context of weaker rock showing TWC strengths substantially greater than UCS. Meier *et al.* (Meier et al., 2013) presented a detailed assessment of borehole diameter and scale effect, making reference to the data in (Cuss et al., 2003). An excellent summary of laboratory test data including CSL prediction from TWC and field log parameters was presented by Khaksar *et al*. (2018). The microstructural and macroscopic shear expression of failure under a wide range of true-triaxial loadings for two high porosity sandstones (UCS of 56 MPa and 30 MPa, respectively) up to high confinements was presented by Ma and Haimson (Ma & Haimson, 2016).

1.3 Numerical models of solids production

To tackle the modelling of the erosive effect of increasing flow velocities creating seepage forces, (Ghassemi & Pak, 2015) coupled a numerical approach based on the Lattice Boltzmann Method (LBM) and Discrete Element Method (DEM) in a 2D fluid flow simulation of deformable particulate media. They showed that a critical flow velocity is required in order to erode the cavity, and that confining stress will supress the erosion. A number of models that couple CFD with DEM have been presented in the last year, *e.g.* (Song et al., 2020) which includes a validation against experimental data.

(Duan & Kwok, 2016) used PFC, a DEM code, to model the propagation of borehole breakouts in model representations of an isotropic rock and an anisotropic shale (UCS ~75 MPa). A range of realistic breakout features with explicit growth of bond breakages were shown, and hole size effects matching experiments are discussed. The RFPA damage model code has also been used to visualise discrete cells that represent damaged or failed elements surrounding compressed boreholes, showing borehole breakout-like patterns (Li et al., 2020).

For the solids-only simulations including effective stresses, pore fluid pressure and poroelasticity, (Younessi & Khaksar, 2016) used the Abaqus code for the FEM solver while (Papamichos & Furui, 2019) use the code Geo3D to obtain the plastic strain at TWC failure. (Wang et al., 2020) have also used the DEM code PFC, but coupled it with the FEM code FLAC to extend the domain out towards the far field. The models of pore collapse in sandstones with porosities of 35-40% and compaction band propagation are impressive. One drawback of DEM modelling of brittle solids is the fracture representation is not as realistic as with FEM and FDEM methods.

With the purpose to model rock fracture processes, and with specific application to tunnels and boreholes, (Shen et al., 2014) developed the boundary element – displacement discontinuity method code FRACOD, which uses fracture mechanics criteria for fracture. However, the expression of crack growth with progressive deformation is less successful as this approach is less suited to model post-peak fragment interactions. The combined finite-discrete element method (FDEM) is better suited to model the transformation of intact continuous rock to discretely fracturing and fragmenting rock under complex boundary stresses and loading histories. Where the confining stresses are higher, the fracturing becomes more distributed within yielding zones, and the discrete shearing by brittle elastic deformation is expressed macroscopically as plastic strain. The FDEM model proposed for simulating solids production in this project is presented in Section 2.

(Mohamad-Hussein & Ni, 2018) included an elastic-plastic damage model with dilatant volumetric plastic strain, which was implemented in the VISAGE finite element code. They also presented a single-phase fluid-coupled model that determines the rate of solids production. The numerical model was illustrated with a complete sand production process analysis tool, *i.e.,* sand formation condition prior to production, drawdown pressure, initial mechanical properties, initial pore pressure and pre-production stress.

The Finite-Discrete Element Method (FDEM) approach was invented thirty years ago by Antonio Munjiza, and has been used extensively to simulate the failure and fragmentation of rocks and geological formations over the past fifteen years; see for example the Special Issue on Combined Finite Discrete Element Method and Virtual Experimentation, October 2020, https://link.springer.com/journal/40571/volumes-and-issues/7-5, which includes four papers from our group.

As explained in the introduction to this report, this discontinuum approach does not require the implementation of sophisticated rock-type-specific constitutive models, as the macroscopic mechanical behaviour of rocks before and after failure can be captured by calibrating the input parameters in the FDEM simulations. These parameters can be optimised for specific rock types by means of standard mechanical tests (*e.g.,* the triaxial test data that were provided for the F6 reservoir). In the case of carbonates, soft and weak rocks can be represented in FDEM modelling by the choice of "low" mechanical parameters as optimised from standard mechanical tests on reservoir-specific carbonate rock specimens. Macroscopic plastic deformation can be accommodated in the FDEM framework with localised shear and tensile cracks. Further development of the FDEM constitutive model can be conducted to incorporate volumetric plastic deformations due to the pore collapse in high confinement regimes.

1.2 Solids production in carbonate formations

Most of the literature on sand and solids production over the last three decades has focussed on theory and experience with breakdown of reservoir sandstones in varying degrees of consolidation and cementation, from weak sands to strong well-cemented sandstones. However, the problems associated with subsidence during depletion in the weak carbonate reservoirs of Sarawak Malaysia prompted early investigations by van Ditzhuijzen *et al.* (1984), and Mah and Draup (2004). More recently, Dudley *et al.* (2009) characterised the reservoir carbonates as highly compacting, with a discussion of subsidence rates in the context of a field-scale numerical model considering gas-water contact and water weakening of the carbonates, having learned from the experiences in the North Sea Ekofisk chalk. They used a modified Cam clay associative plasticity constitutive model, with the Mohr-Coulomb parameters taken to be a cohesion of 2.4 MPa and an angle of internal friction of 27 degrees, and a mean stress cap of about 17 MPa to capture the pore collapse behaviour, from which the numerical model predicted subsidence acceleration.

A significant literature exists on strength behaviour of carbonates, *e.g.* Mogi (1971), but this work mostly describes rocks that are much stronger than the ones in question. Hickman (2004) provides a review of elasto-(visco)-plastic constitutive models appropriate to chalk, which includes models very similar to the one used by Dudley *et al.* (2009), and which therefore might be suitable for continuum modelling of Luconia platform carbonates, in the event that they show similar chalk-like properties. A wellbore stability analysis for chalk reservoir rock by Hajiabadi *et al.* (2020) included a rate-dependent response in the constitutive model, with M-C shear failure and pressure cap implemented in ABAQUS. They compared wellbore continuous plastic deformation in their numerical model with experiments, which clearly exhibited breakout behaviour showing shear fracture and fragmentation as the actual expression of their borehole response during testing, as shown below. This lends some support to the discontinuum approach we are adopting for the modelling in this research.

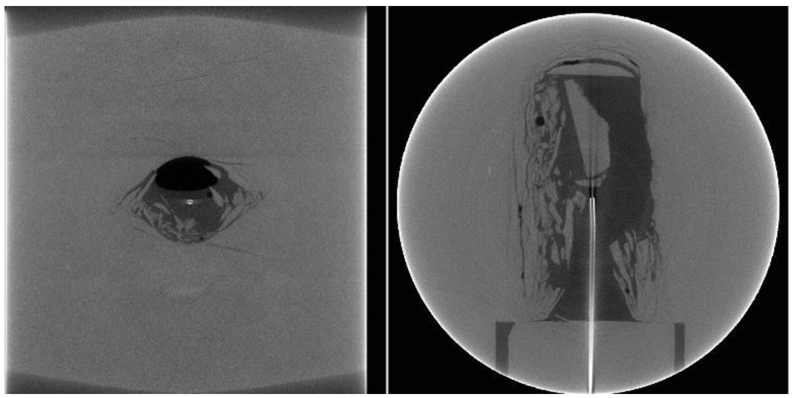

Figure 1. CT image visualization of the breakout in chalk, from Hajiabadi *et al.* (2020)

Relevant experimental research on breakout initiation, growth, and stabilisation behaviour specifically with Alabama, Cordova Cream, and other limestones, by Haimson and Song (1993) and Hendrick and Haimson (1994), led to theoretical and numerical models of how a dog-eared type breakout might amplify and stabilise.

Research on solids production associated with rock properties of chalky carbonates in the oil and gas reservoirs of Indonesia were discussed by (Nurhandoko & Listyobudi, 2018). They suggested that engineers may benefit from following currently preferred theory and management practice for sand production, focussing on standard TWC experiments that monotonically ramp up the axial and radial confinement isotropically. However, they emphasised that carbonates may behave with specific differences to sandstones. The novelty of their work is that they reported on strength results of two carbonate specimens for the TWC test, which failed at 5 and 12 MPa, together with continuous data on the rates of mass accumulated from inner wall deterioration, and lateral and volumetric strain during testing. They discussed the early observed sand production phenomena at very low confining stress, and the changes of slope and rapid increase in solid production rate at a certain applied confining pressure just prior to and signalling final specimen failure. Total confining stress triggering the last phase of rapid sanding for these TWC specimens with zero internal pressure were taken to be of significance for further use in the strategy for pumping and bottom hole drawdown pressure design.

The basic theory underpinning the solids production prediction modelling alluded to by (Nurhandoko & Listyobudi, 2018) is probably very similar to that outlined by (Asadi et al., 2016). This case history from Malaysia is for sandstone lithologies with injector and producer wells in an oil reservoir. The strength of the target rock, well trajectory, reservoir pressure, and production conditions are inputs to a prediction model that considers the *in-situ* stress and pore pressure evolution during depletion, and critical strength multipliers based on TWC test results. Sand-free production was predicted for the existing wells and new wells, based on careful deduction of the *in-situ* stress history during poro-elastic depletion of the well site considering a range of A-factors (depletion constants) to estimate the change in horizontal stress. The vulnerability to sand production was considered for perforated completions, assessing all possible orientations for a well of given azimuth and deviation from the vertical. The sand-free prediction was born out by field observations, and it was suggested that for a reservoir with pressures drawn down to 0.7 MPa at the end of life, perforations could still be drilled at any angle.

A follow-up paper (Asadi et al., 2017) applied a similar rationale to a high-porosity carbonate gas reservoir in offshore Vietnam, with the aim to assess whether the "widely used" approach to solids production prediction is also applicable to porous, chalky carbonates. Both cased-perforated and open-hole field examples were analysed using 1D geomechanical models from log interpretations and were considered risk-free from solids production problems using current reservoir pressures and drawdowns. This conclusion was consistent with field observations. The prediction model suggested that drawdowns of 1.4 MPa higher could be tolerated at the time of writing in 2017, but zero drawdown would be required to prevent solids production if reservoir pressure drops by a further ~5 MPa. They concluded that the need for strict control measures would be very important for the new infill wells being drilled in recent years.

There is little mention of potential mechanisms and modifications to the widely-used prediction model that might be necessary for the specific case of carbonate reservoirs. However, Asadi *et al.* (2017) includes rarely published laboratory test results on Carbonates from South East Asia reservoir settings, including UCS and TWC data. The TWC collapse failure strength data for these carbonates represented, characterised as vuggy and of high-variability and high-porosity, range from 6.3 to 19 MPa (900-2700 psi), with porosity ranging from 16 to 35%. Extensive use is made of correlations derived for UCS versus acoustic velocity, porosity and density and for TWC test values versus acoustic velocity and porosity. Clearly, TWC is needed for the model prediction method rather than UCS, and so log-derived data are converted to TWC values directly. In the target rock formation for the Vietnam field under investigation (NCS reservoirs), the TWC value according to the correlations from log data suggest the minimum strength lithology has TWC of only ~6.3 MPa, with 10% of the limestones having TWC <7.2 MPa. A scatter plot of the TWC/UCS ratio as a function of UCS was not presented, which would have been interesting, since extensive data for sandstones shows that for weak sandstones of UCS ~5 MPa, the TWC is apparently typically three to six times greater.

The data of (Asadi et al., 2016) (see Fig. 5 from their paper) for weak carbonates based on seven samples (it is not clear whether one point represents a single specimen or the average of a sample) is inconclusive, given such a small data set, but suggests a different trend and therefore a different type of yielding behaviour may exist for this vuggy limestone compared with sandstone data of similar porosity and strength. This point is not highlighted in the paper, perhaps because of the scattered and rather sparse data. The best fit curves that were presented suggest that for porosity increasing from 15 to 35%, the UCS falls from ~34 MPa to ~5 MPa, while TWC falls from ~15 MPa to ~7 MPa. This corresponds to a TWC/UCS ratio of between 1 to 2, when UCS ~ 5 MPa, which suggests that the mechanism operating to potentially strengthen weak highly porous sandstones in borehole wall rock under the reservoir conditions of higher confinement may be different than for carbonates. Further rock mechanics testing of samples from Luconia platform reservoir carbonates will be useful to establish more reliable relationships between TWC and logged parameters, and how UCS and triaxial strength parameters contribute to TWC yield phenomena for weak carbonate samples.

A case study of solids production analysis from a carbonate reservoir in Oman for open-hole completions was presented by (AL-Aamri et al., 2020). This is an interesting case history, as the analysis of when drawdown exceeds that predicted for solids production is compared with the performance log of when electrical submersible pumps (ESPs) were malfunctioning for five different wells. The carbonate UCS values of between 30 and 35 MPa were evaluated from correlations including with ROP during drilling. These rocks are some five times stronger than the carbonates from the Luconia Platform. With these stronger carbonates from Oman, a maximum drawdown of 3 MPa was recommended for wells with intervals depleted to or below reservoir pressure of ~10 MPa, to ensure that wells were free from carbonate solids production.

An extensive literature review has been conducted, and it has been determined that only a very limited number of publications have covered the problem of solids production from carbonate reservoirs in South-East Asia. Further papers on solids production from experiences in known chalk and chalky limestone reservoirs such as the North Sea, have also proven difficult to find, with the one notable interesting exception by the Danish group (Hajiabadi *et al.,* 2020) mentioned above.

1.3 Further comparison of Asadi et al (2017) with compiled sandstone data (PSBR)

It is apparent from close inspection of the data points in Fig A1 that few cores tested in (a) are from the exact same rock horizons and porosity values as those cores tested in (c) and therefore a scatter plot of UCS vs TWC is not appropriate. The UCS data is derived from points indicated in blue in the logs together with the zero confining pressure results from the multistage triaxial indicated in red. Only a few of the blue points appear to correspond with the TWC points indicated in brown. With a word of caution, it is possible to draw some inferences from the relatively strong independent relationships of UCS and of TWC with porosity as shown in (a) and (c). By substituting porosity values at regular intervals from 15% to 35%, into each of the best fit equations in units of psi, the relations

$$
\begin{aligned}
&TWC = 52\ UCS^{0.439} && \text{psi units} \\
&TWC/UCS = 52\ UCS^{-0.561} && \text{psi units} \\
&TWC/UCS = 3.187\ UCS^{-0.561} && \text{MPa units} \qquad \text{(A1)}
\end{aligned}
$$

were obtained. This is a small data set on vuggy weak carbonates from Vietnam. It is important to make clear the TWC values reported are for saturation in oil (not brine) and the UCS saturation state is not detailed in the paper. With interest in solids production, the TWC initial yield stress rather than the TWC collapse stress, which can be quite significantly greater, see Fig A2, is the TWC value reported here. Note also that the carbonate rocks are with vugs but essentially fine grained compared with sandstones and therefore grain size effects in the carbonates may have less influence.

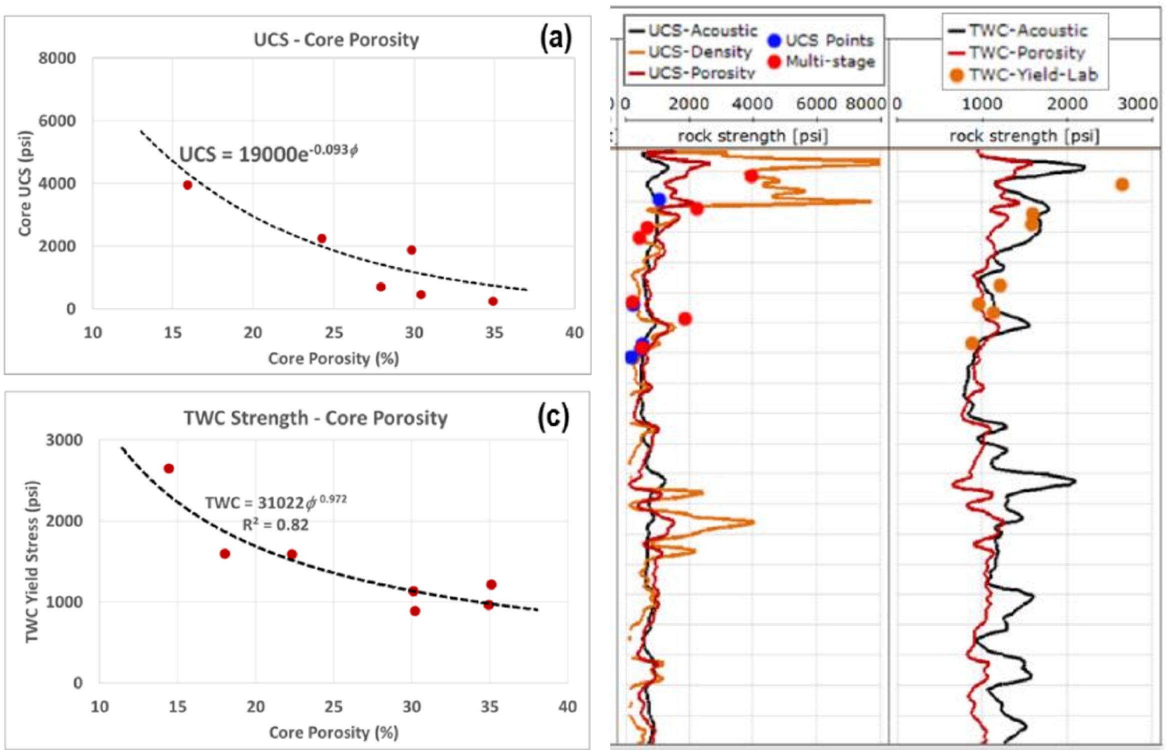

Figure A1 UCS,TWC, Porosity and Log Data (Asadi et al 2017)

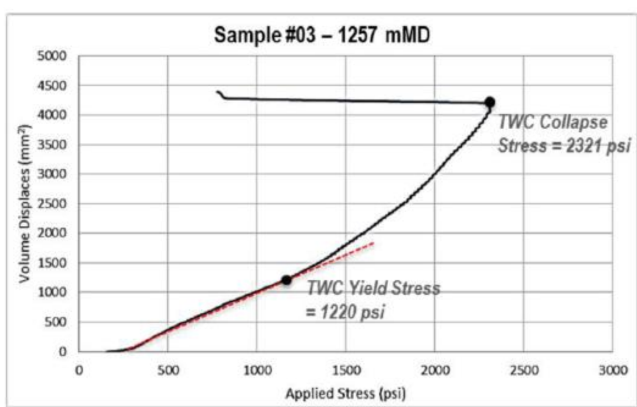

Figure A2 Detection of TWC yield stress and final TWC collapse stress in ATWC test (Asadi et al 2017).

Having in mind the above cautionary points with which the carbonate results are now compared with PSBR's compiled data for sandstones (TWC and UCS test saturation conditions and criteria for failure stress in TWC are not considered), Fig A3 shows clearly a different lower TWC/UCS trend for the carbonates reported by Asadi et al (2017), even if TWC values were increased by a factor to account for differences between collapse and yield criteria.

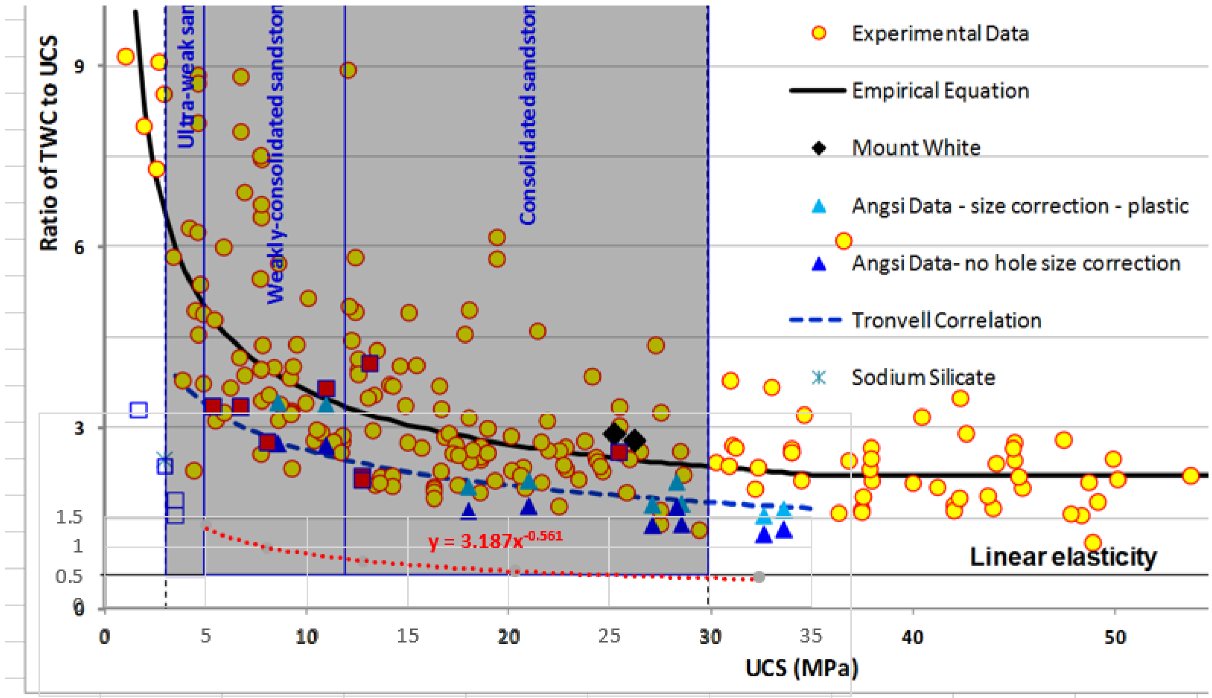

Figure A3 PRBS sandstone data with Carbonate trend (red dotted line) deduced from Asadi et al., (2017) superimposed.

1.4 In-situ stress and geological setting in the Luconia platform

The regional tectonic setting and present-day stress orientations off NW Borneo are described by (King et al., 2010) and in relation to faulting by Ting *et al.* (2011). A full-basin evolution and sedimentological model for the Miocene reefs in the South China sea has been given by Mathew *et al.* (2020), which helps explain the presence of these massive reef limestones. Of particular interest and relevance to the Petronas carbonate field in question is the local *in-situ* stress analysis of Gland *et al*. (2015), which provides analysis of *in-situ* stress magnitude and direction from logs in the Kinabalu field Malaysia that point towards very low differential horizontal stresses in the Normal Fault regime. The stress regime for the Kinabalu field is normal, with a Q ~ [0.3-0.5] and a stress anisotropy ratio of σ_H/σ_h ~ [1.11-1.14].

2 The combined finite-discrete element method for the simulation of solids production

Section 2 includes an introduction to FDEM software, 2D FDEM large-strain code implementation and verifications, implementation and verification of pore-pressure effects on poroelastic response, and a novel boundary condition implementation scheme needed to speed up the simulations. Finally, workflow input and FDEM results output for progressive fragmentation and borehole wall-rock failure and collapse, are illustrated.

2.1 FDEM software

Algorithms for the combined finite-discrete element method (FDEM) started to be proposed in the 1990s. Developments and applications of the FDEM method have been carried out after the release of the open-source Y-code by Munjiza (2004). Imperial College London, in a collaboration with Queen Mary University of London, released the first open source FDEM code for geoscience problems in the late 2000s (Munjiza et al., 2010; Xiang et al., 2009). This code, initially named Virtual Geoscience Simulation Tools (VGeST), has been recently upgraded to simulate more general mechanical problems, and renamed 'Solidity' (Applied Modelling and Computation Group (AMCG) at Imperial College London, 2018). The key features of the FDEM framework are the following: (a) compute the contact detection and interactions and motion of bodies, (b) calculate the stresses and deformations, and (c) compute the transition from continua to discontinua when fragmentation occurs. Details of the theoretical underpinnings of the algorithms used to calculate the stresses and trajectories of deformable bodies can be found in (Farsi, Xiang, et al., 2020; Munjiza, 2004) and Farsi *et al.* (2020). The calculation of stresses and deformation is based on standard linear elastic FEM methods. More background on the implementations of the smeared crack model to simulate the solid fragmentation and solid production in FDEM will be discussed in this section, and more details can also be found in (Farsi, Bedi, et al., 2020; Munjiza et al., 1999).

The transition from a continuous domain to a discontinuous domain during rock fragmentation is carried out through fracture initiation and propagation processes. The progressive fracture mechanisms implemented in the code are idealised with a distributed micro-crack zone, a bridging zone, and a traction free macro-crack zone. This is based on the assumption that the stress-strain curve consists of a hardening branch (before the peak) and a strain-softening part (where the stress decreases with the strain increasing), as illustrated in Fig. 2.

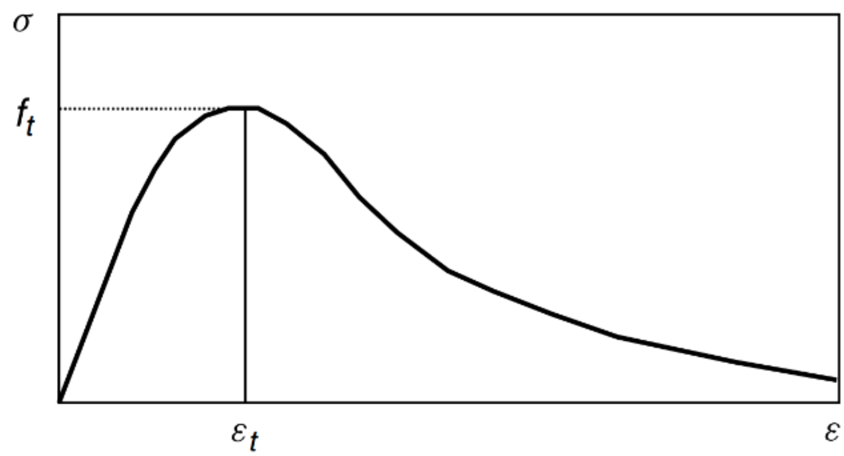

Figure 2: Objective stress-strain curve to be modelled (Munjiza, 2004).

Figure 3 shows the strain-softening relation that has been implemented in the code through the constitutive law of the joint elements in terms of stress and displacements. The strain-softening part is also defined in terms of stress and displacements in order to avoid the ill-posedness of the problem generated by a stress-strain definition. The area under the graph in Fig. 3 is the energy release rate (G_c), *i.e.* the energy dissipated in order to extend the surface of the crack. G_c is also equal to twice the surface energy, which quantifies the disruption of bonds that occur when a surface is created.

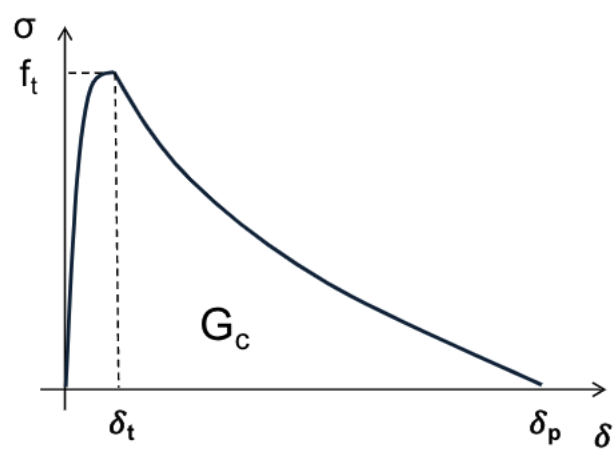

Figure 3: Strain-softening defined in terms of displacements (Farsi, Bedi, et al., 2020).

The relationship between stresses and displacements is modelled through a single crack model: when the size of separation is zero the bonding stress is equal to the tensile strength (f_t), implying that the separation begins only after reaching this stress value equal to f_t. Once the separation starts to increase, there will be a decrease in bonding stress. When it reaches a limit value of separation (δ_p), the bonding stress tends to zero. In the actual implementation of this model, the separation of adjacent element edges is assumed in advance by introducing joint elements and describing the topology of adjacent elements with different nodes. As no two elements share any nodes, the continuity between elements is enforced through the penalty function method. Before the bonding stress reaches the tensile strength, its value is given by eq. (1), where δ_t is the separation corresponding to when the bonding stress is equal to the tensile strength $\delta_t = 2hf_t/p$), h is the size of that particular finite element, and p is the penalty parameter:

(1)

After the bonding stress has reached the tensile strength, the strain-softening law described in terms of stress and displacements is given by eq. (2), with a heuristic scaling function representing an approximation of the experimental stress-displacement curves, and the parameters a = 0.63, b = 1.8, and c = 6 are obtained from the interpolation of experimental stress displacement curves. These parameters only define the shape of the softening curve, which is then stretched, depending on the material properties of the material (*i.e.*, the energy release rate and the tensile strength). However, the heuristic curve that was implemented in the first Y-code was derived from direct tension experiments on concrete samples (Evans & Marathe, 1968). Other materials have been tested to obtain a more representative softening curve shape, such as granite, *e.g.* see (Rougier et al., 2014). The variable D is given by eq. (3), and the complete relationship for the normal bonding stress as a function of separation can be written as shown in eq. (4).

(2)

(3)

(4)

3 An efficient finite-discrete element workflow for the simulation of circular boreholes in poroelastic media

3.1 Introduction

Understanding the role of fluid flow in the deformation and fragmentation behaviour of porous media remains an open challenge for several research and engineering fields, such as geothermal energy enhancement, oil and natural gas recovery, CO_2 sequestration, long-term disposal of nuclear waste, just to name a few.

Although a generic modelling strategy can be developed for a wide range of such problems, some applications still require an individual approach to be applicable. The aim of this work is to present an effective computational implementation of a continuum-discontinuum formulation for drilled rock masses under the effects of a steady state fluid flow and in-situ stress confinements.

3.2 Governing equations

3.2.1 Fluid flow

The basic law governing the flow of fluids through porous media is Darcy's law:

$$q = \frac{Q}{A} = \frac{-k}{\mu}\frac{d\mathrm{P}}{dx} \tag{1.2.1.1}$$

in which q is the fluid flux [m^3/s], Q is the volumetric flowrate [m^3/s], P is the "corrected" fluid pressure [Pa]. When x is a direction perpendicular to the gravitational field, P is exactly the fluid pressure. The constant k is the permeability [m^2], μ is the fluid viscosity [Pa s], and A is the cross-sectional area that is crossed by the fluid flux in the sample [m^2]. The term $\frac{d\mathrm{P}}{dx}$ represents the change in fluid pressure when moving through the sample in the direction x.

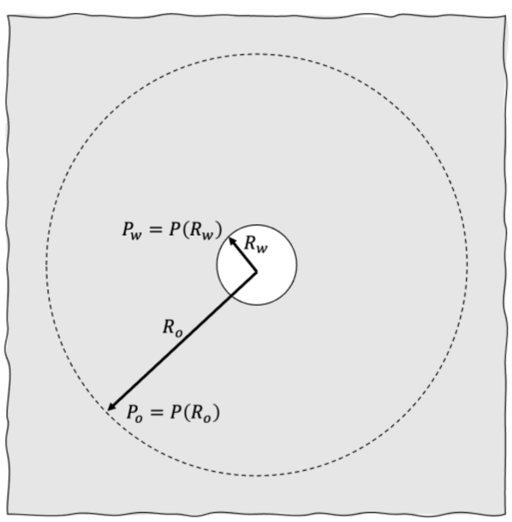

Figure 1.2.1.1: Schematic of a circular borehole that has been drilled into a porous material with homogeneous and isotropic permeability.

Consider a circular borehole that has been drilled into a porous material with homogeneous and isotropic permeability. Assume further that this formation has a constant pressure at its outer boundary, and a constant flow of fluid is moving into the borehole. The domain under consideration in Fig. f1 has thickness H and horizontal permeability k, and the circular borehole has radius R_w. At some radius R_o, the pressure remains at its undisturbed value P_o (*i.e.* $P(R_o) = P_o$). The pressure of the fluid inside the borehole and on its walls is constant and equal to P_w (*i.e.* $P(R_w) = P_w$). The rate at which the fluid must be removed from the borehole to maintain a steady-state condition in the system is Q. Assuming that the pressure distribution in this system has reached a steady state (in which $dP/dt = 0$), the flow rate into the reservoir at $R = R_o$ must be equal the flow rate into the wellbore at $R = R_w$. Given the cylindrical symmetry of this system, Darcy's law can be written for flow in the R direction as follows:

$$Q = \frac{-kA}{\mu}\frac{dP}{dR} \tag{1.2.1.2}$$

The cross-sectional area normal to the flow, at a radial distance R from the centre of the borehole, is $2\pi RH$ (*i.e.* a cylindrical surface of height H and perimeter $2\pi R$), so

$$Q = \frac{-2\pi kH}{\mu} R \frac{dP}{dR} \tag{1.2.1.3}$$

By separating the variables, we obtain

$$\frac{dR}{R} = \frac{-2\pi kH}{\mu Q} dP \tag{1.2.1.4}$$

and integration from the outer boundary ($R = R_o$), to a generic location R gives

$$\int_{R_o}^{R} \frac{dR}{R} = -\int_{P_o}^{P} \frac{2\pi kH}{\mu Q} dP \tag{1.2.1.5}$$

We now substitute the integration boundaries and rearrange the terms to find

$$\ln\left(\frac{R}{R_o}\right) = \frac{-2\pi kH}{\mu Q}(P - P_o) \tag{1.2.1.6}$$

$$P(R) = P_o - \frac{\mu Q}{2\pi kH}\ln\left(\frac{R}{R_o}\right) \tag{1.2.1.7}$$

Equation (1.2.1.7) is an analytical solution for the fluid pressure profile in the porous material as a function of the distance from the centre of the borehole (R), the undisturbed value of fluid pressure ($P_o = P(R_o)$) and the term $\frac{\mu Q}{2\pi kH}$. We now substitute $P(R_w) = P_w$ in the previous equation with the aim of obtaining a solution for the fluid pressure profile solely in terms of the undisturbed (P_o) and borehole wall (P_w) pressures, without requiring knowledge of the rock or fluid properties, or the flowrate:

$$P_w = P_o - \frac{\mu Q}{2\pi kH}\ln\left(\frac{R_w}{R_o}\right) \tag{1.2.1.8}$$

$$\frac{\mu Q}{2\pi kH} = \frac{(P_o - P_w)}{\ln(R_w/R_o)} \tag{1.2.1.9}$$

Finally, we substitute this expression for $\frac{\mu Q}{2\pi kH}$ into the fluid pressure profile in Equation (1.2.1.7) to obtain

$$P(R) = P_o - \frac{(P_o - P_w)}{\ln(R_w/R_o)}\ln(R/R_o) \tag{1.2.1.10}$$

To check the boundary conditions, note that at $R = R_o$, we have ln $(R/R_o) = \ln (R_o/R_o) = \ln (1) = 0$, and Equation (1.2.1.10) gives $P = P_o$. At the borehole walls, where $R = R_w$, the two log terms cancel out, and Equation (1.2.1.10) gives $P = P_o - (P_o - P_w) = P_w$.

3.2.2 Poroelastic media

The initial location of a material point P in an elastic or poroelastic medium can be denoted by $P = (x, y, z)$, where (x, y, z) are the point coordinates relative to a Cartesian coordinate system. After the solid is deformed, the new location of that material point will be $P^* = (x^*, y^*, z^*)$. The vector that points from the new position to the old position is the displacement vector **u**, defined as

$$\mathbf{u}(P) = P - P^* = (u, v, w) = (x, y, z) - (x^*, y^*, z^*) \tag{1.2.2.1}$$

The diagonal terms (*i.e.,* normal strains) and off diagonal terms (*i.e.,* shear strains) of the strain tensor are defined as follows:

$$\varepsilon_{xx} = \frac{\partial u}{\partial x};\ \varepsilon_{yy} = \frac{\partial v}{\partial y};\ \varepsilon_{zz} = \frac{\partial w}{\partial z} \tag{1.2.2.2}$$

$$\begin{aligned} \varepsilon_{xy} &= \varepsilon_{yx} = \frac{1}{2}\left(\frac{\partial u}{\partial y} + \frac{\partial v}{\partial x}\right),\ \varepsilon_{xz} = \varepsilon_{zx} = \frac{1}{2}\left(\frac{\partial u}{\partial z} + \frac{\partial w}{\partial x}\right) \\ \varepsilon_{yz} &= \varepsilon_{zy} = \frac{1}{2}\left(\frac{\partial v}{\partial z} + \frac{\partial w}{\partial y}\right) \end{aligned} \tag{1.2.2.3}$$

For a linear elastic medium, the relation between the components of the strain tensor and the diagonal terms (*i.e.*, normal stresses) and off diagonal terms (*i.e.,* shear stress) of the stress tensor is defined in terms of the shear modulus (G) and Poisson ratio (v):

$$\begin{aligned} \varepsilon_{xx} &= \frac{1}{2G}\left[\tau_{xx} - \frac{v}{(1+v)}\left(\tau_{xx} + \tau_{yy} + \tau_{zz}\right)\right] \\ \varepsilon_{yy} &= \frac{1}{2G}\left[\tau_{yy} - \frac{v}{(1+v)}\left(\tau_{xx} + \tau_{yy} + \tau_{zz}\right)\right] \\ \varepsilon_{zz} &= \frac{1}{2G}\left[\tau_{zz} - \frac{v}{(1+v)}\left(\tau_{xx} + \tau_{yy} + \tau_{zz}\right)\right] \\ \varepsilon_{xy} &= \tau_{xy}/2G,\ \varepsilon_{xz} = \tau_{xz}/2G,\ \varepsilon_{yz} = \tau_{yz}/2G \end{aligned} \tag{1.2.2.4}$$

These relations can be written in matrix form and its inverse, as follows:

$$\boldsymbol{\varepsilon}^{\boldsymbol{e}} = \frac{1}{2G}\boldsymbol{\tau}^{\boldsymbol{e}} - \frac{v}{2G(1+v)}\text{trace }(\boldsymbol{\tau}^{\boldsymbol{e}})\mathbf{I} \tag{1.2.2.5}$$

$$\boldsymbol{\tau}^{\boldsymbol{e}} = 2\text{G}\,\boldsymbol{\varepsilon}^{\boldsymbol{e}} + \frac{2Gv}{1-2v}\text{trace}(\boldsymbol{\varepsilon}^{\boldsymbol{e}})\,\mathbf{I} \tag{1.2.2.6}$$

In the case of a macroscopically isotropic poroelastic medium, a pore pressure increment will lead to an equal extension along each of three mutually orthogonal directions, without generating any shear strains, as a pore fluid cannot sustain a shear stress under static conditions and therefore no shear traction can be transmitted to the pore walls. The parameter C_{bp} is the compressibility coefficient that defines the volumetric strain resulting from an applied pore pressure ($C_{\mathrm{bp}} = \frac{1}{V_{\mathrm{b}}^{i}}\left(\frac{\partial V_{\mathrm{b}}}{\partial P_{\mathrm{p}}}\right)_{P_{\mathrm{c}}}$). Since the total bulk volumetric strain resulting from the pore pressure is $-C_{\mathrm{bp}}P_{\mathrm{p}}$, the coefficient that relates each macroscopic longitudinal strain to the pore pressure must be $-C_{\mathrm{bp}}/3$. Hence, a term $-C_{\mathrm{bp}}P_{\mathrm{p}}/3$ must be added to each of the longitudinal strains, yielding

$$\boldsymbol{\varepsilon}^{\boldsymbol{p}} = \frac{1}{2G}\boldsymbol{\tau}^{\boldsymbol{e}} - \frac{\nu}{2G(1+\nu)}\text{trace}\ (\boldsymbol{\tau}^{\boldsymbol{e}})\mathbf{I} - \frac{C_{\text{bp}}}{3}P_{\text{p}}\mathbf{I} \tag{1.2.2.7}$$

Note that when moving from Equation (1.2.2.5) to equation (1.2.2.7), the stresses and strains at each material point become an average over an "infinitesimal" region of the poroelastic medium that encloses many pores.

Because of the superposition principle, the compressibility of the solid material, *i.e.* the rock grains, (C_{m}) is equal to the difference of the compressibility of the bulk material, *i.e.,* the ensemble of rock grains and pores, due to the confining pressure (C_{bc}) and the pore pressure (C_{bp}):

$$C_{\text{m}} = C_{\text{bc}} - C_{\text{bp}} \tag{1.2.2.8}$$

Equation (1.2.2.7) can therefore be written in terms of the Biot coefficient α:

$$\alpha = 1 - \frac{C_{\text{m}}}{C_{\text{bc}}} = 1 - \frac{K_{\text{bc}}}{K_{\text{m}}} = 1 - \frac{K}{K_{\text{m}}} \tag{1.2.2.9}$$

Noting that $C_{\text{bc}} = 1/K$, where K is the macroscopic bulk modulus, this leads to

$$\boldsymbol{\varepsilon}^{\boldsymbol{p}} = \frac{1}{2G}\boldsymbol{\tau}^{\boldsymbol{e}} - \frac{\nu}{2G(1+\nu)}\text{trace}\ (\boldsymbol{\tau}^{\boldsymbol{e}})\mathbf{I} - \frac{\alpha}{3K}P_{\text{p}}\mathbf{I} \tag{1.2.2.10}$$

Taking the trace of both sides of Equation (1.2.2.10) yields

$$\text{trace}\ (\boldsymbol{\varepsilon}^{\boldsymbol{p}}) = \frac{(1-2\nu)}{2G(1+\nu)}\text{trace}\ (\boldsymbol{\tau}^{\boldsymbol{e}}) - \frac{\alpha}{K}P_{\text{p}} \tag{1.2.2.11}$$

The equation for the stresses in terms of the strains is found by inverting Equation (1.2.2.5) with the aid of Equation (1.2.2.11):

$$\boldsymbol{\tau}^{\boldsymbol{p}} = 2\text{G}\ \boldsymbol{\varepsilon}^{\boldsymbol{e}} + \lambda\,\text{trace}(\boldsymbol{\varepsilon}^{\boldsymbol{e}})\,\mathbf{I} + \alpha P_{\text{p}}\mathbf{I} \tag{1.2.2.12}$$

By comparing Equation (1.2.2.6) and Equation (1.2.2.12) it is possible to write

$$\boldsymbol{\tau}^{\boldsymbol{p}} = \boldsymbol{\tau}^{\boldsymbol{e}} + \alpha P_{\text{p}}\mathbf{I} \tag{1.2.2.13}$$

The meaning of this equation can also be seen as the equilibrium of the stresses acting of the infinitesimal volume of poroelastic material, as shown in Figure 1.2.2.1.

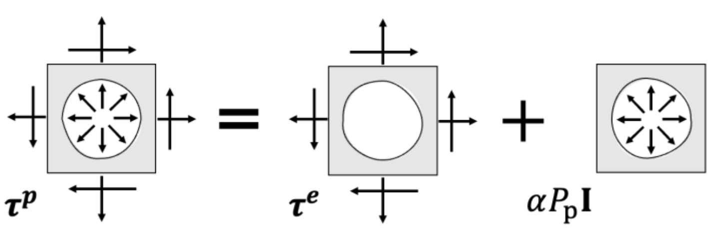

Figure 1.2.2.1: Schematic of the equilibrium between the stresses acting on an infinitesimal volume of poroelastic material.

Let B denote an infinitesimal volume of poroelastic material and let ∂B be the outer boundary of this volume. Newton's second law states that the total force applied to this volume is equal to the mass of the body multiplied by its acceleration ($\boldsymbol{F} = m\ \boldsymbol{a}$). The total force acting on this volume ($\boldsymbol{F}$) consists of the sum of all the body forces that act over the internal portions of the volume ($\iiint_B \rho \boldsymbol{F}_b\ \text{d}V$), plus the resultant force due to all the surface tractions that act over the outer boundary of the volume ($\iint_{\partial B}$ (p_t $\mathbf{n}$) dA). The momentum of volume B in the right-hand side of Newton's second law can be calculated by integrating the product of the density of the material (ρ) and acceleration ($\frac{\partial^2 \mathbf{u}}{\partial t^2}$) over the volume B. This yields to the following equilibrium condition:

$$\iiint_B \boldsymbol{F}_b \, \mathrm{d}V + \iint_{\partial B} (\mathrm{p}_t \, \mathbf{n}) \, \mathrm{d}A = \iiint_B \rho \frac{\partial^2 \mathbf{u}}{\partial t^2} \, \mathrm{d}V \qquad (1.2.2.14)$$

Since B is an infinitesimal volume, the surface tractions acting on each face are given by the components of the stress tensor $\boldsymbol{\tau}$. This allows us to rewrite the previous expression as:

$$\iiint_B \boldsymbol{F}_b \, \mathrm{d}V + \iint_{\partial B} (\boldsymbol{\tau}^{\boldsymbol{p}} \cdot \mathbf{n}) \, \mathrm{d}A = \iiint_B \rho \frac{\partial^2 \mathbf{u}}{\partial t^2} \, \mathrm{d}V \qquad (1.2.2.15)$$

To obtain an expression with volume integrals, but without surface integrals, the divergence theorem can be used to express the integral of the surface tractions over the boundaries in terms of the divergence of the surface tractions integrated over the volume of B ($\iint_{\partial B}$ $(\boldsymbol{\tau}^{\boldsymbol{p}} \cdot \mathbf{n})$ dA = $\iiint_B$ div($\boldsymbol{\tau}^{\boldsymbol{p}}$) d$V$). This yields

$$\iiint_B \boldsymbol{F}_b \, \mathrm{d}V + \iiint_B \mathrm{div}(\boldsymbol{\tau}^{\boldsymbol{p}}) \, \mathrm{d}V = \iiint_B \rho \frac{\partial^2 \mathbf{u}}{\partial t^2} \, \mathrm{d}V \qquad (1.2.2.16)$$

Bringing all the terms on the right-hand side of the equation yields

$$\iiint_B \left[\boldsymbol{F}_b + \mathrm{div}(\boldsymbol{\tau}^{\boldsymbol{p}}) \;-\; \rho \frac{\partial^2 \mathbf{u}}{\partial t^2}\right] \mathrm{d}V = 0 \qquad (1.2.2.17)$$

Since Newton’s second law must hold for any material point, regardless on the choice of the boundaries of integration that defines the infinitesimal volume under consideration, the previous equality must be equivalent to

$$\boldsymbol{F}_b + \mathrm{div}(\boldsymbol{\tau}^{\boldsymbol{p}}) \;-\; \rho \frac{\partial^2 \mathbf{u}}{\partial t^2} = 0 \qquad (1.2.2.18)$$

The term div($\boldsymbol{\tau}^{\boldsymbol{p}}$) can be calculating using Equation (1.2.2.13) and noting that the pore pressure P_p is a scalar field. Moreover div$\left(\alpha P_\mathrm{p} \mathbf{I}\ \right)$ is therefore equal to the gradient of αP_p, which leads to

$$G\nabla^2\mathbf{u} + (\lambda + G)\nabla(\nabla \cdot \mathbf{u}) - \rho\ddot{\mathbf{u}} = -\boldsymbol{F}_b - \boldsymbol{F}_p \qquad (1.2.2.19)$$

where Newton’s notation has been used for the second derivative with respect to time of the displacement vector field ($\frac{\partial^2 \mathbf{u}}{\partial t^2} = \ddot{\mathbf{u}}$) and $\boldsymbol{F}_p = \alpha\Delta P_\mathrm{p}$.

The term $G\nabla^2\mathbf{u} + (\lambda + G)\nabla(\nabla \cdot \mathbf{u})$ represents the elastic forces ($\boldsymbol{F}_e$) that are generated inside the poroelastic material to equilibrate the inertial forces ($\rho\ddot{\mathbf{u}}$) and the other externally applied loads ($\boldsymbol{F}_b$ and $\boldsymbol{F}_p$). The previous expression can therefore be written in a more compact form as

$$\boldsymbol{F}_e - \rho\ddot{\mathbf{u}} = -\boldsymbol{F}_b - \boldsymbol{F}_p \qquad (1.2.2.20)$$

3.3 Combined finite-discrete element implementation

3.4 Internal and external nodal forces

What follows shows how the internal forces ($\boldsymbol{F}_e$) in Equation (1.2.2.20) are calculated for each finite element node following the combined finite-discrete element framework. When employing a constant strain triangular finite element, the deformation over the element is the linear function shown as follows:

$$\begin{aligned} x_c &= \alpha_x x_i + \beta_x y_i \\ y_c &= \alpha_y x_i + \beta_y y_i \end{aligned} \tag{1.3.1.1}$$

where x_c and y_c represent current coordinates (deformed configuration), and x_i and y_i represent the initial coordinates (undeformed configuration).

The deformation over the domain of the finite element is expressed in terms of the deformation at nodes of the triangle and the deformation at nodes of a triangle is defined by the initial nodal coordinates corresponding to the initial configuration, and current nodal coordinates corresponding to the deformed configuration. The easiest way to calculate the deformation gradient for a constant strain triangular finite element is to use the deformed initial frame. Using this frame, the matrix of the deformation gradient tensor can be calculated with

$$\mathbf{F} = \begin{bmatrix} \frac{\partial x_c}{\partial \hat{x}_i} & \frac{\partial x_c}{\partial \hat{y}_i} \\ \frac{\partial y_c}{\partial \hat{x}_i} & \frac{\partial y_c}{\partial \hat{y}_i} \end{bmatrix} = \begin{bmatrix} x_{1c} - x_{0c} & x_{2c} - x_{0c} \\ y_{1c} - y_{0c} & y_{2c} - y_{0c} \end{bmatrix} \tag{1.3.1.2}$$

where x_c and y_c are the current global coordinates given in the global frame $(\mathbf{i}, \mathbf{j})$ while $\hat{x}$ and $\hat{y}$ are the current coordinates expressed using the initial frame. For each finite element, x_{1c} and y_{1c} are the current global coordinates of node 1, x_{2c} and y_{2c} are the current global coordinates of node 2 and x_{0c} and y_{0c} are the current global coordinates of node 0**.** It is worth noting that node 0 in the initial configuration coincides with the origin of the initial frame. The matrix of the velocity gradient tensor can be calculated in a similar fashion as:

$$\mathbf{L} = \begin{bmatrix} \frac{\partial v_{xc}}{\partial \hat{x}_i} & \frac{\partial v_{xc}}{\partial \hat{y}_i} \\ \frac{\partial v_{yc}}{\partial \hat{x}_i} & \frac{\partial v_{yc}}{\partial \hat{y}_i} \end{bmatrix} = \begin{bmatrix} v_{1xc} - v_{0xc} & v_{2xc} - v_{0xc} \\ v_{1yc} - v_{0yc} & v_{2yc} - v_{0yc} \end{bmatrix} \tag{1.3.1.3}$$

where v_{ixc} is the current velocity of node i in the direction of the global base vector **i**, while v_{iyc} is the current velocity of node i in the direction of the global base vector **j**.

The matrix of the left Cauchy–Green strain tensor (**B**) can be calculated as

$$\mathbf{B} = \mathbf{F}\,\mathbf{F}^{\boldsymbol{T}} \tag{1.3.1.4}$$

and the matrix of the rate of deformation tensor (**D**) can be obtained from the velocity gradient as

$$\mathbf{D} = \frac{1}{2}(\mathbf{L} + \mathbf{L}^{\boldsymbol{T}}) \tag{1.3.1.5}$$

The Cauchy stress tensor is constant within each finite element and can be calculated as

$$\mathbf{T} = 2\mathrm{G}\,\mathbf{E} + \frac{2Gv}{1-2v}\,\mathrm{trace}(\mathbf{E})\,\mathbf{I} + 2\mu\,\boldsymbol{D} \tag{1.3.1.6}$$

in terms of the shear modulus (G) and Poisson's ratio (v). The term $2\mu\boldsymbol{D}$ is added to reduce numerical instabilities and can be interpreted as a viscous damping, where μ is the viscous damping coefficient.

The traction force over each of the three edges of the triangle can be calculated using the normal on the edge of the deformed configuration ($\mathbf{m}$). The traction on each edge i is given by

$$\mathbf{s}_i = \mathbf{T}\,\mathbf{m}_i \tag{1.3.1.7}$$

Edge traction for each of the three edges of the deformed configuration is distributed in equal proportion to each of the nodes belonging to a particular edge. The equivalent nodal force is calculated for each node by summing the contribution coming from each edge connected to the node, as shown below:

$$\mathbf{F}_{\boldsymbol{e}} = \sum_{i=1}^{2} \frac{1}{2} \mathbf{s}_i \tag{1.3.1.8}$$

The external forces in the RHS of Equation (1.2.2.20) are calculated for each finite element node. The externally applied loads ($\boldsymbol{F}_b$ and $\boldsymbol{F}_p$) are simply calculated based on the coordinates of the centroid of each finite element and then equally redistributed to the three nodes of each finite element. The distance of the centroid of each finite element from the centre of the borehole (R_c) is calculated from

$$\mathrm{R}_c = \sqrt[2]{\tilde{x}^2 + \tilde{y}^2} \tag{1.3.1.9}$$

where $\tilde{x}$ and $\tilde{y}$ are the coordinates of the centroid in the global frame of reference.

The vector $\boldsymbol{F}_p$ for each finite element can be calculated with Equation (1.3.1.10) where $\bar{\mathbf{r}}$ is a unit vector pointing towards the centre of the borehole, that can be calculated with Equation (1.3.1.11):

$$\boldsymbol{F}_p = \alpha\, \Delta P_{\mathrm{p}} = -\alpha \frac{(P_O - P_W)}{\ln\left(\frac{R_W}{R_O}\right)} \left(\frac{R_C}{R_O}\right) \overline{\mathbf{r}_{\boldsymbol{c}}} \tag{1.3.1.10}$$

$$\overline{\mathbf{r}_{\boldsymbol{c}}} = -\frac{(\tilde{x}, \tilde{y})}{\mathrm{R}_c} \tag{1.3.1.11}$$

3.5 Modelling examples and verification

3.5.1 FDEM models

In the following simulation examples, a circular hole of diameter 1 m is considered. It is assumed that the pore fluid flow has reached a steady state and has an undisturbed pore pressure at 3 m from the centre of the well. For this reason, in the simulation only a 6 m outer diameter disc of the rock formation was considered, as shown in Figure 1.4.1.1.

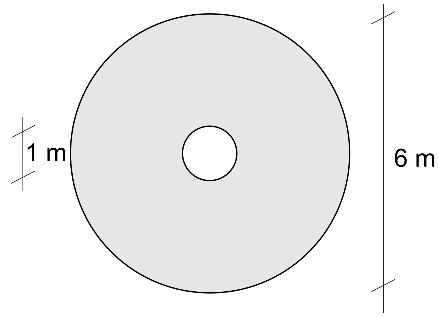

Figure 1.4.1.1: Geometry of the simulated well.

The following three scenarios have been considered: (a) an unconfined well subjected to an undisturbed pore fluid pressure of 1 MPa; (b) a well under a hydrostatic confinement of 1 MPa and no pore fluid pressure; (c) a well under a hydrostatic confinement of 1 MPa and subjected to an undisturbed pore fluid pressure of 1 MPa. The three cases are shown in Figure 1.4.1.2.

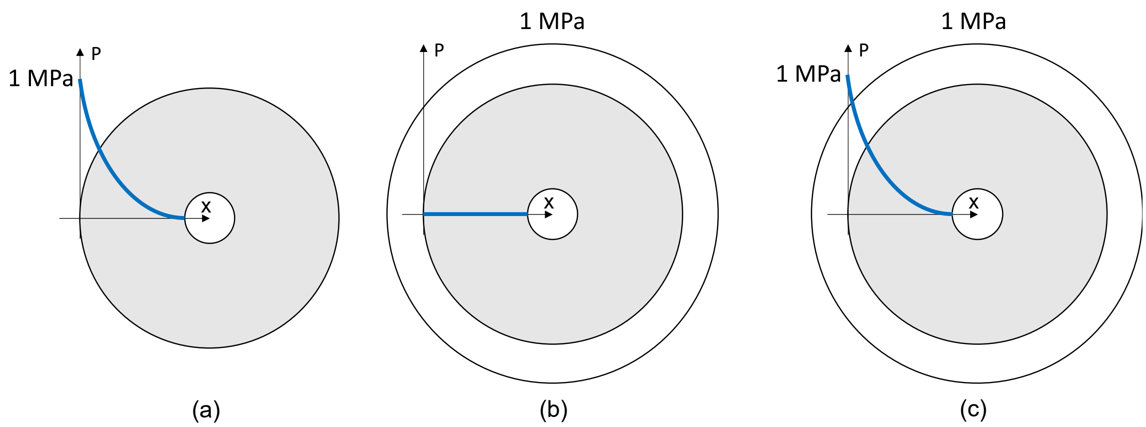

Figure 1.4.1.2: Three simulated scenarios: (a) an unconfined well subjected to an undisturbed pore fluid pressure of 1 MPa; (b) a well under a hydrostatic confinement of 1 MPa and no pore fluid pressure; (c) a well under a hydrostatic confinement of 1 MPa and subjected to an undisturbed pore fluid pressure of 1 MPa.

An unstructured triangular mesh is used to discretize the simulated domain, as shown in Figure 1.4.1.3. The average element edge size is 75 mm. The mechanical parameters that were employed on the simulation of the three test cases are shown in Table 1.4.1.1. The time step size used in the simulations is 5.4 x10^{-8} seconds.

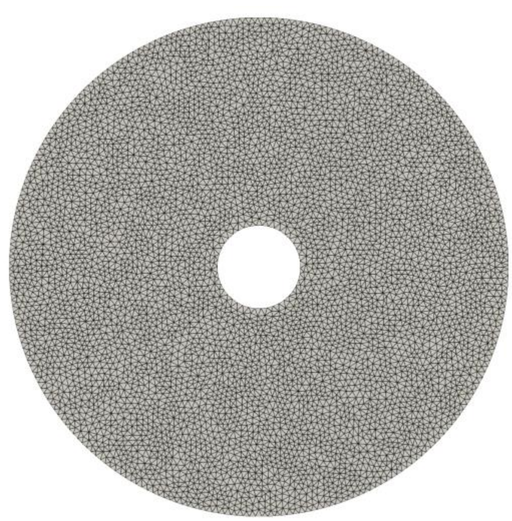

Figure 1.4.1.3: FDEM mesh discretisation for the three simulated scenarios.

Table 1.4.1.1: Mechanical parameters used in the simulations.

Density [kg / m^3]	2580
Young's modulus [GPa]	4.7
Poisson's ratio [/]	0.26
Penalty term (Normal) [N/m]	2.35E+11
Penalty term (Tangential) [N/m]	2.35E+12

3.5.2 Governing equation solution with Firedrake

Firedrake is a Python-based FEM automation package that uses PETSc to solve partial differential equations. Firedrake accepts equations written in their weak form and automatically generates and assembles the matrices that are necessary to solve the partial differential equations as a linear system of equations.

The equations obtained in the previous sections were solved with continuous linear Galerkin test functions. In this case, only a quarter of the domain was simulated, as shown in Figure 1.4.2.1. The symmetry of this problem with respect to the vertical and horizontal axes is imposed by blocking the horizontal displacements in the top right boundary segment and by blocking the vertical displacements in the bottom left segment of the domain, as shown in Figure 1.4.2.2. The same three scenarios that have been presented in the previous section were also considered: (a) an unconfined well subjected to an undisturbed pore fluid pressure of 1 MPa; (b) a well under a hydrostatic confinement of 1 MPa and without pore fluid pressure; (c) a well under a hydrostatic confinement of 1 MPa and subjected to an undisturbed pore fluid pressure of 1 MPa. The three cases are also shown in Figure 1.4.2.2.

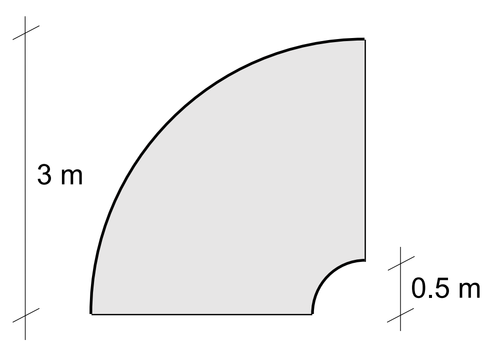

Figure 1.4.2.1: Geometry of the domain simulated with Firedrake.

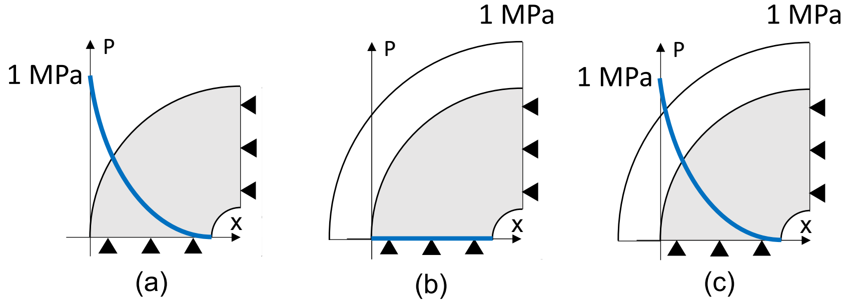

Figure 1.4.2.2: Three simulated scenarios: (a) an unconfined well subjected to an undisturbed pore fluid pressure of 1 MPa; (b) a well under a hydrostatic confinement of 1 MPa and no pore fluid pressure; (c) a well under a hydrostatic confinement of 1 MPa and subjected to an undisturbed pore fluid pressure of 1 MPa.

A semi-structured triangular mesh is used to discretize the simulated domain, as shown in Figure 1.4.2.3. The average element edge size is 25 mm. The same mechanical parameters that were employed for the FDEM simulations were also used to simulate the three test cases with Firedrake; see Table 1.4.1.1.

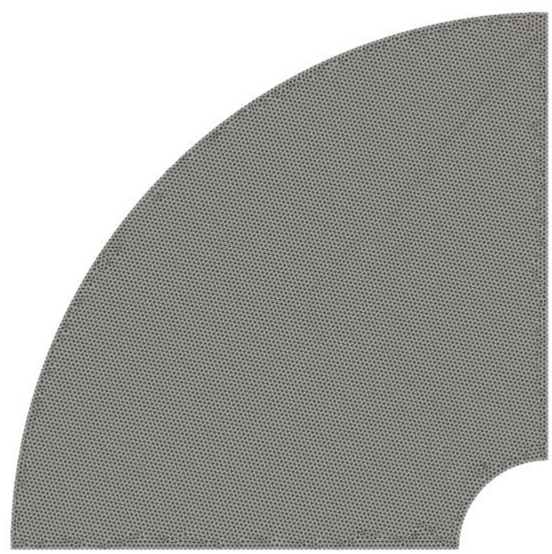

Figure 1.4.2.3: Firedrake mesh discretisation for the three simulated scenarios.

3.5.3 Comparison of the results

The simulations were run with the FDEM code described in the previous sections and the results were compared to the simulations results obtained from solving the same partial differential equations using Firedrake. The results from FDEM simulations are in agreement with the results from Firedrake for the three scenarios. Figures 1.4.3.1–9 show a comparison of the displacement, first principal stress and second principal stress fields obtained from FDEM and Firedrake.

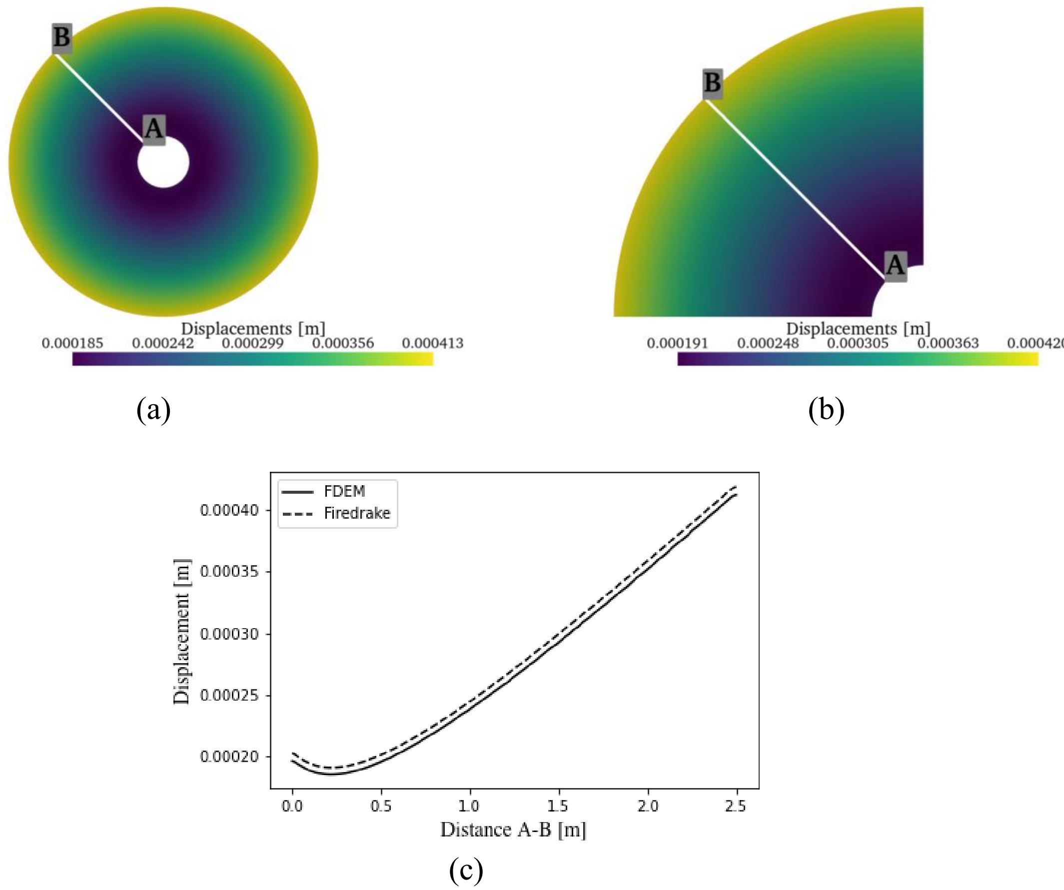

Figure 1.4.3.1: Displacement field in the first scenario: comparison between the solution from (a) FDEM and (b) Firedrake. (c) Displacement over the A-B line in the solution from FDEM (continuous line) and Firedrake (dashed line).

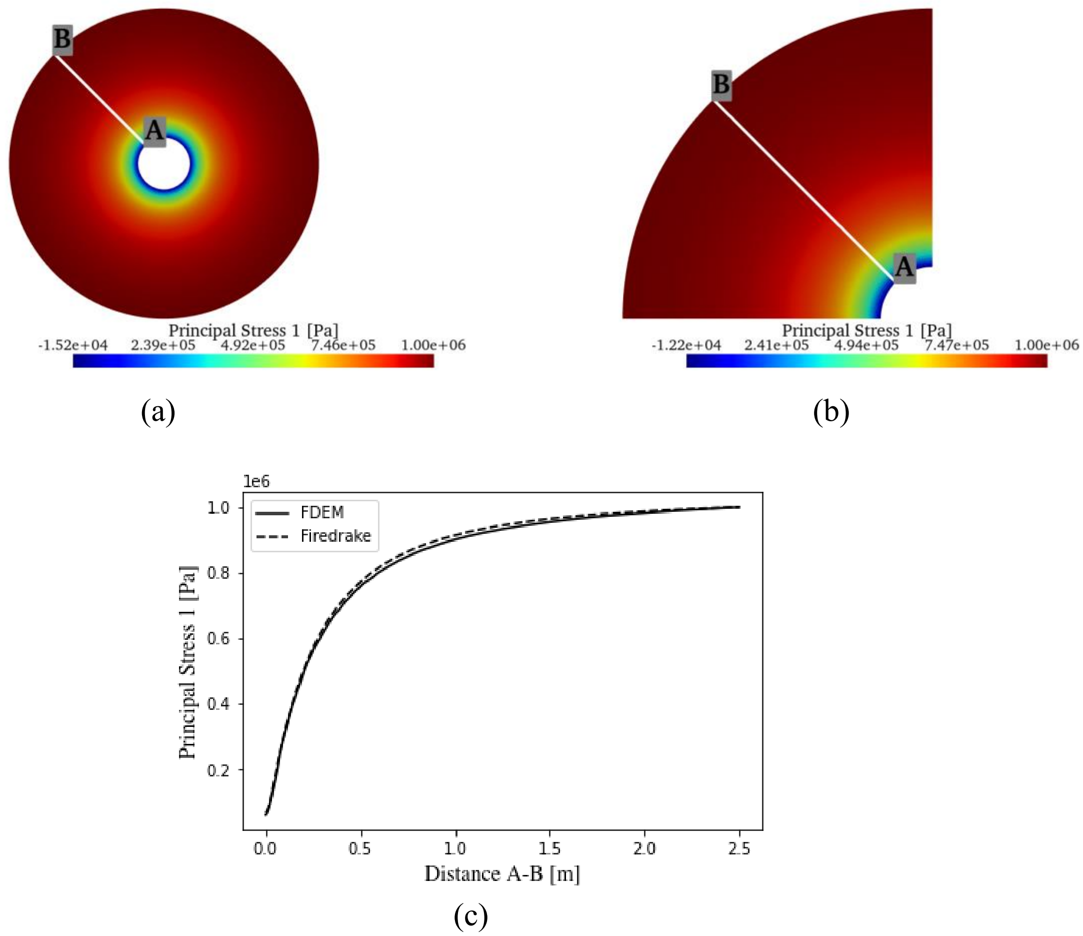

Figure 1.4.3.2: First principal stress field in the first scenario: comparison between the solution from (a) FDEM and (b) Firedrake. (c) First principal stress over the A-B line in the solution from FDEM (continuous line) and Firedrake (dashed line).

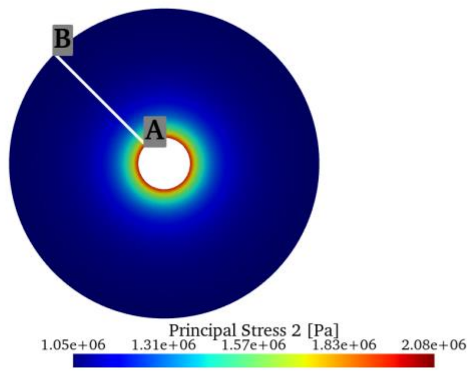

(a)

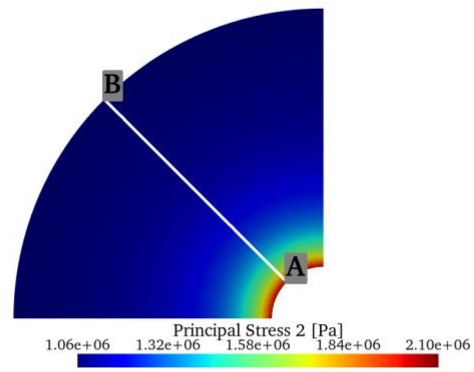

(b)

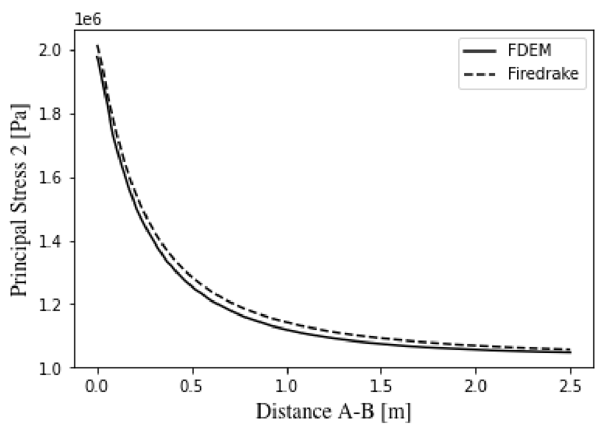

(c)

Figure 1.4.3.3: Second principal stress field in the first scenario: comparison between the solution from (a) FDEM and (b) Firedrake. (c) Second principal stress over the A-B line in the solution from FDEM (continuous line) and Firedrake (dashed line).

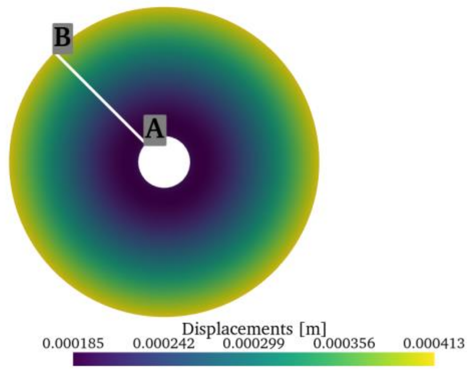

(b)

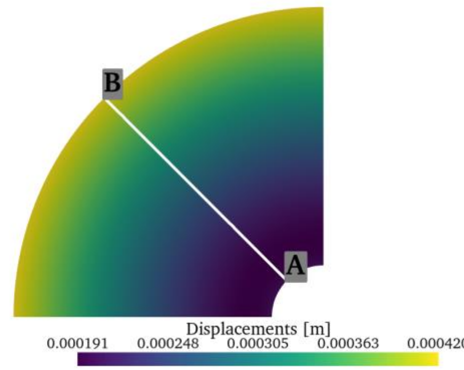

(b)

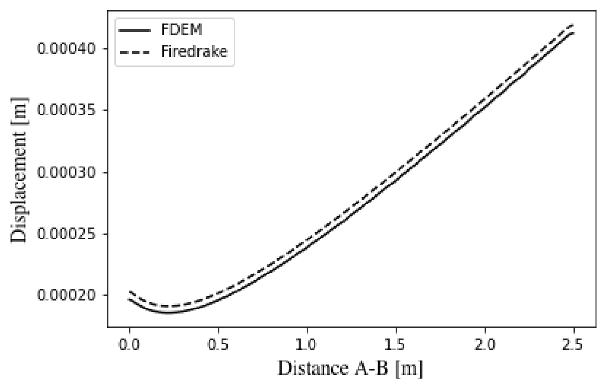

(c)

Figure 1.4.3.4: Displacement field in the second scenario: comparison between the solution from (a) FDEM and (b) Firedrake. (c) Displacement over the A-B line in the solution from FDEM (continuous line) and Firedrake (dashed line).

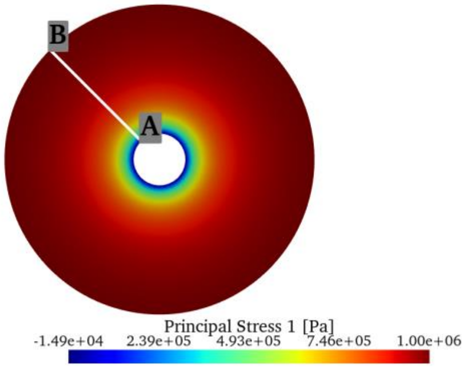

(b)

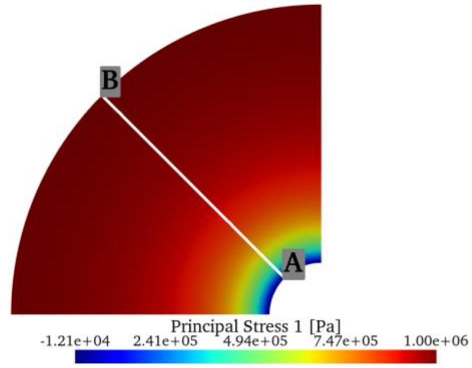

(b)

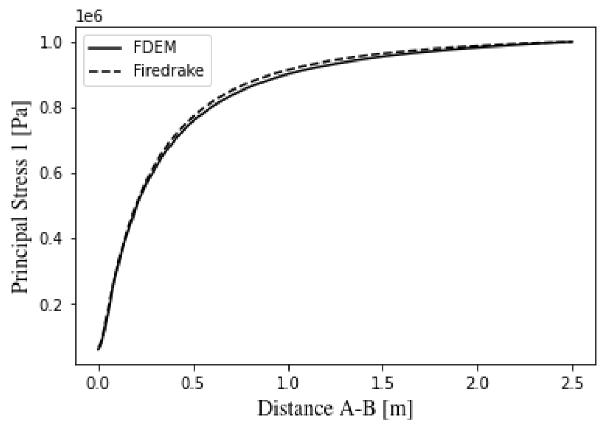

(c)

Figure 1.4.3.5: First principal stress field in the second scenario: comparison between the solution from (a) FDEM and (b) Firedrake. (c) First principal stress over the A-B line in the solution from FDEM (continuous line) and Firedrake (dashed line).

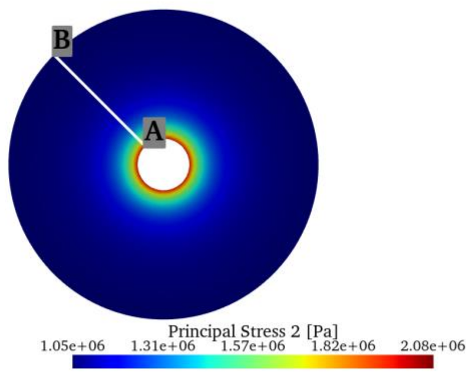

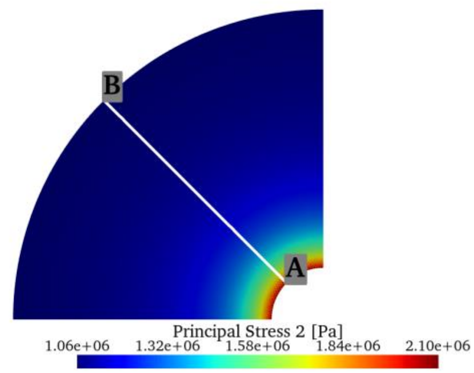

z

(b) (b)

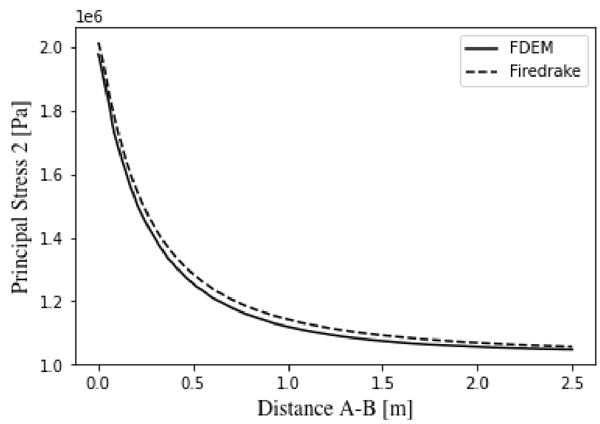

(c)

Figure 1.4.3.6: Second principal stress field in the second scenario: comparison between the solution from (a) FDEM and (b) Firedrake. (c) Second principal stress over the A-B line in the solution from FDEM (continuous line) and Firedrake (dashed line).

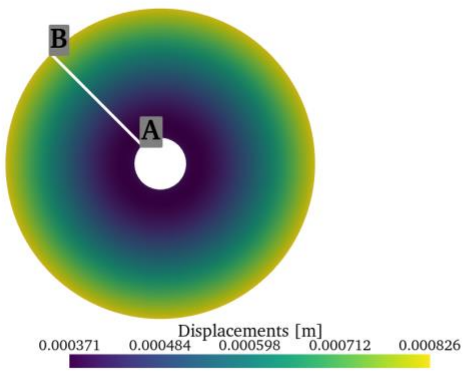

(c)

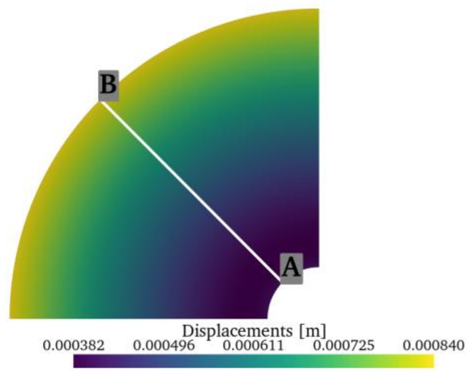

(b)

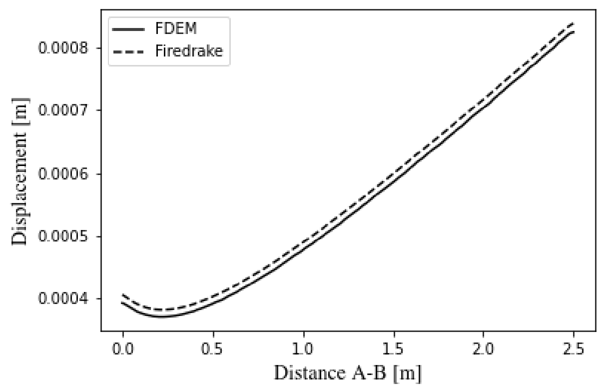

(c)

Figure 1.4.3.7: Displacement field in the third scenario: comparison between the solution from (a) FDEM and (b) Firedrake. (c) Displacement over the A-B line in the solution from FDEM (continuous line) and Firedrake (dashed line).

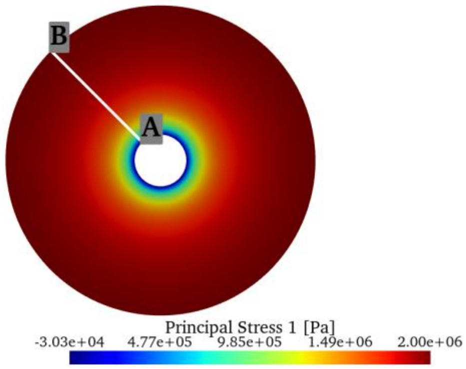

(c)

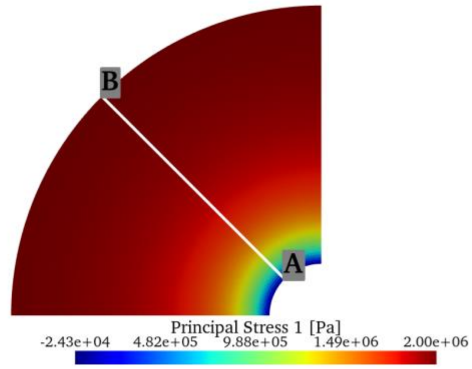

(b)

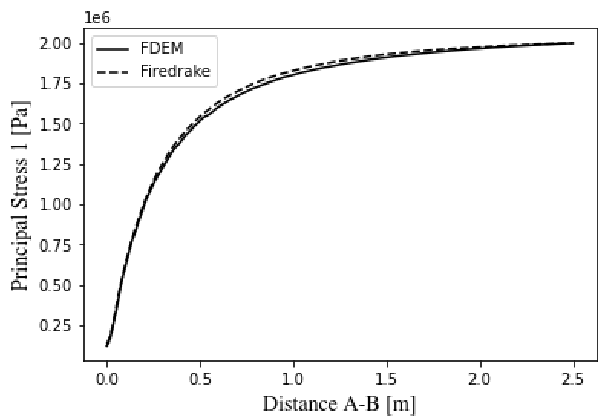

(c)

Figure 1.4.3.8: First principal stress field in the third scenario: comparison between the solution from (a) FDEM and (b) Firedrake. (c) First principal stress over the A-B line in the solution from FDEM (continuous line) and Firedrake (dashed line).

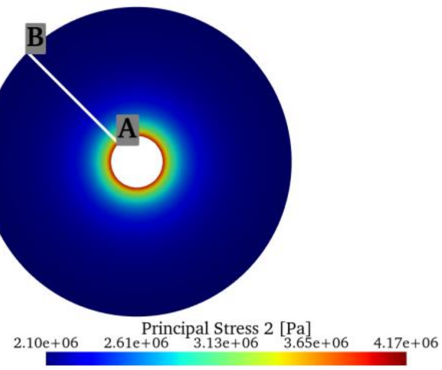

(c)

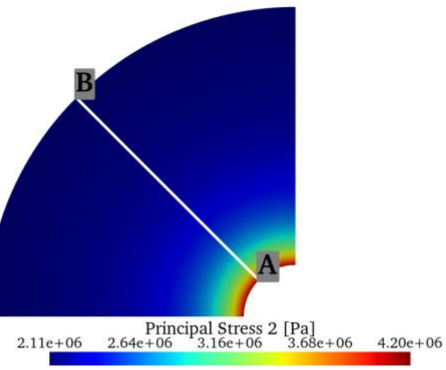

(b)

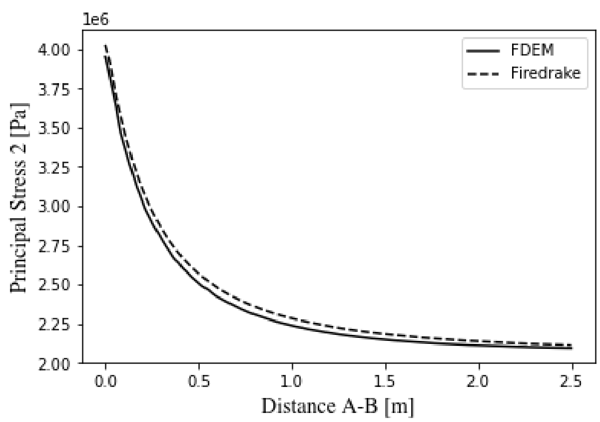

(c)

Figure 1.4.3.9: Second principal stress field in the third scenario: comparison between the solution from (a) FDEM and (b) Firedrake. (c) Second principal stress over the A-B line in the solution from FDEM (continuous line) and Firedrake (dashed line).

3.5.4 Conclusions

An effective computational implementation of a continuum-discontinuum formulation for drilled rock masses under the effects of a steady state fluid flow and in-situ stress confinements have been presented and validated. The results from the proposed FDEM methodology of three different scenarios were compared to the simulations results obtained from solving the same partial differential equations using Firedrake. The comparison show that the results agree, to a high degree.

4 Testing and analysis for the mechanical characterisation and solid production estimation of carbonate rocks

4.1 Introduction

The following section contains the mechanical testing that will be used for the determination of the numerical parameters and the validation of the numerical model in the next chapter.

4.2 Mechanical characterisation

With the aim of characterising the mechanical properties of the TWC rock samples, several cylindrical samples were extracted from the available coring materials used in the TWC tests. The geometries of the samples are reported in Table 2.2.1. Brazilian disc tests, unconfined uniaxial tests, and triaxial tests were performed in the FTL.

Table 2.2.1: Geometries of the samples used for the mechanical characterization of the ATWC carbonate rock samples. (a) Unconfined uniaxial tests, (b) Brazilian disc tests, (c) single stage triaxial tests.

Well	Sample	Core Depth (feet)	Saturation Fluid	Length (mm)	Diameter (mm)	Dry Mass (g)	Wet Mass (g)	Bulk Volume (cm3)	Pore Volume (cm3)	Sat. Bulk Density (g/cc)	L:D	Porosity (%)	Unconfined Compressive Strength (psi)
F6-2	1	4426.50	Formation Brine	76.03	37.92	147.35	178.53	85.86	30.36	2.079	2.0:1	35.4	617
F6-2	2	4441.40	Formation Brine	76.02	37.90	158.19	184.82	85.76	25.93	2.155	2.0:1	30.2	602
F6-2	3	4491.60	Formation Brine	75.89	37.92	171.33	189.36	85.71	17.56	2.209	2.0:1	20.5	1611
F6-2	4	4524.80	Formation Brine	75.96	37.92	180.42	194.70	85.79	13.90	2.270	2.0:1	16.2	1817
F6-2	5	4551.80	Formation Brine	73.08	37.86	146.07	169.14	82.27	22.46	2.056	1.9:1	27.3	764
F6-2	6	4572.50	Formation Brine	75.89	37.96	150.18	177.46	85.89	26.56	2.066	2.0:1	30.9	757
F6-2	7	4654.65	Formation Brine	75.94	37.93	186.30	200.95	85.81	14.26	2.342	2.0:1	16.6	1923

(a)

Well	Sample	Core Depth (ft)	Saturation Fluid	Length (mm)	Diameter (mm)	Sat. Bulk Density (g/cc)	Brazilian Tensile Strength (psi)
F6-2	1A	4427.30	Formation Brine	20.32	37.93	1.917	70.1
F6-2	1B	4427.30	Formation Brine	17.88	37.92	1.986	87.1
F6-2	2	4441.40	Formation Brine	19.36	37.92	2.083	52.1
F6-2	3A	4491.70	Formation Brine	19.44	37.91	2.096	107
F6-2	3B	4491.70	Formation Brine	19.37	37.93	2.178	157
F6-2	4A	4524.70	Formation Brine	19.03	37.92	2.048	42.6
F6-2	4B	4524.70	Formation Brine	18.96	37.93	2.172	73.2
F6-2	5	4551.90	Formation Brine	18.79	37.93	2.093	71.6
F6-2	6	4572.60	Formation Brine	19.03	37.89	1.970	70.9
F6-2	7A	4654.55	Formation Brine	18.97	37.91	2.210	123
F6-2	7B	4654.55	Formation Brine	18.99	37.91	2.163	59.8

(b)

Well	Sample Ref	Core Depth (ft)	Porosity (%)	Confinement (psi)	Failure Stress (psi)	Residual Strength (psi)	Young's Modulus (10^6 psi)	Poisson's Ratio	Sat Bulk Density (g/cc)	Length (mm)	Diameter (mm)	L:D
F6-2	1b	4427.30	28.0	435	2483		0.649	0.120	2.202	63.64	25.27	2.5:1
F6-2	1a	4427.30	35.8	725	1743		0.503	-0.051	2.085	63.71	25.26	2.5:1
F6-2	2b	4440.70	33.8	435	2188		0.381	0.112	2.101	63.76	25.28	2.5:1
F6-2	2a	4440.70	34.6	725	2499		0.491	0.143	2.106	63.56	25.26	2.5:1
F6-2	3b	4491.60	30.8	435	3019	2760	0.118	0.017	2.176	63.60	25.27	2.5:1
F6-2	3a	4491.60	26.2	725	3119		0.852	0.142	2.195	63.69	25.28	2.5:1
F6-2	4b	4524.80	32.5	435	1998		0.459	0.219	2.125	63.68	25.30	2.5:1
F6-2	4a	4524.80	22.3	725	3803		1.012	0.103	2.314	63.69	25.31	2.5:1
F6-2	5b	4552.30	32.3	435	2337		0.523	0.093	2.114	60.24	25.24	2.4:1
F6-2	5a	4552.30	27.9	725	2593		0.396	0.148	2.111	63.47	25.23	2.5:1
F6-2	6b	4572.55	35.9	435	1458		0.326	0.188	2.044	63.61	25.27	2.5:1
F6-2	6a	4572.55	27.7	725	2148		0.577	0.145	2.180	62.62	25.29	2.5:1
F6-2	7b	4654.55	21.6	435	3641	3280	0.653	0.088	2.340	61.65	25.28	2.4:1
F6-2	7a	4654.55	30.9	725	3541		0.487	0.181	2.180	62.62	25.29	2.5:1

(c)

4.3 Unconfined uniaxial tests

Seven samples were tested under unconfined uniaxial tests. The sample geometries are reported in Table 2.2.1. The results of the tests in terms of UCS against sample porosity are shown in Figure 2.2.1.1. The UCS values show a linear dependence on porosity, going from a value of about 13.8 MPa for the more competent samples to about 3.5 MPa for the weaker samples.

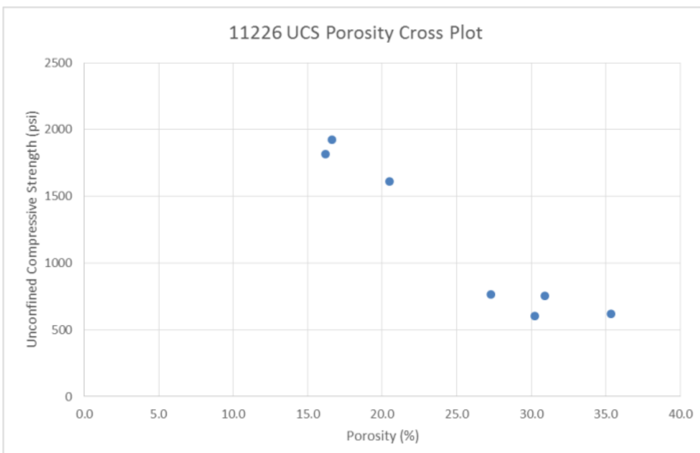

Figure 2.2.1.1: Results of the unconfined compression tests in terms of UCS against sample porosity.

4.4 Brazilian disc tests

A total of eleven cylindrical samples were tested with Brazilian disc tests. The sample geometries are reported in Table 2.2.1. The results of the tests in terms of indirect tensile strength against sample porosity are shown in Figure 2.2.1.2. In principle, a Brazilian disc fails in tensile when a tensile crack begins in the centre of the specimen and propagates towards the two loading plates, forming a straight vertical crack, as shown in Figure 2.2.1.3a. Some of the samples presented different failure modes such as the one shown in Figure 2.2.1.3b. This was probably due to pre-existing cracks and vugs in the samples and the corresponding test results were therefore excluded from the dataset.

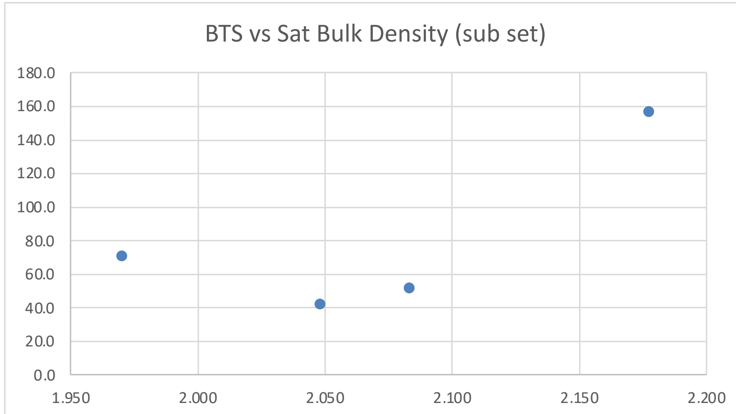

Figure 2.2.1.2: Results of the Brazilian disc tests in terms of indirect tensile strength against sample bulk density.

(a)

(b)

Figure 2.2.1.3: Photograps of two tested sample after Brazilian disc tests: (a) tensile and (b) mixed failure mode.

4.4.1 Single stage triaxial tests

Single stage triaxial tests have been conducted with the aim of characterising the elastic proprieties and shear strength parameters of the carbonate rocks of interest. Figure 2.2.3.1 shows the results of the single stage triaxial tests before and after excluding some of the data. The Mohr-Coloumb failure envelop optimisation is shown in Figure 2.2.3.2. Some example with positive slope for higher porosities (34%) and (b) negative (not acceptable) slope for lower porosities (27%) are also shown. Figure 2.2.3.3 shows the Young's modulus plotted against the porosity of the tested samples. The data is calculated from the results of the single stage triaxial tests.

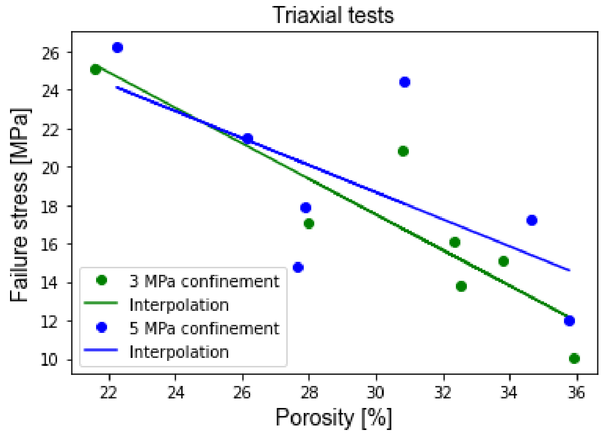

(a)

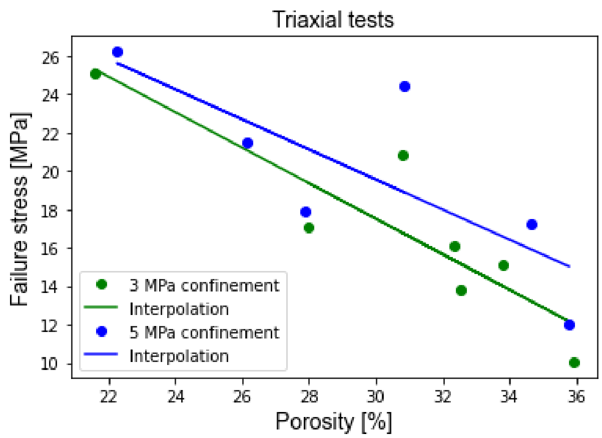

(b)

Figure 2.2.3.1: Results of the single stage triaxial tests. (a) Before and (b) after excluding some of the data.

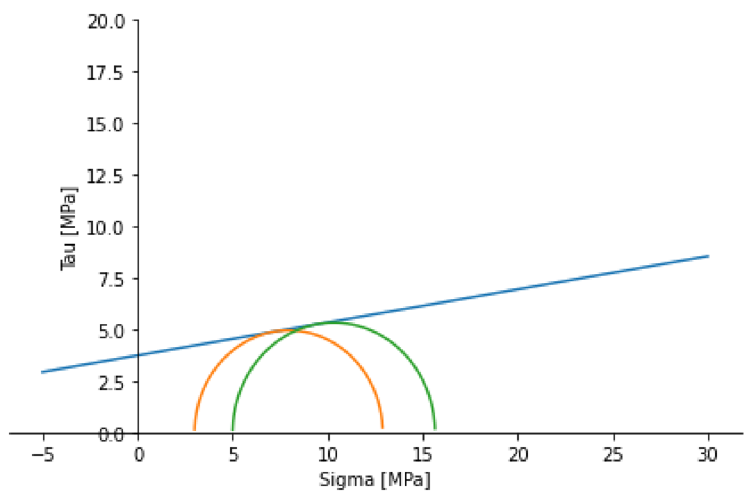

(a)

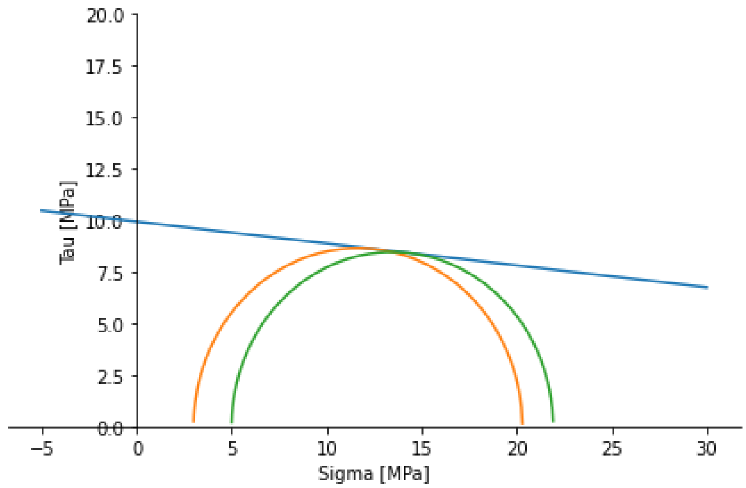

(b)

Figure 2.2.3.2: Mohr-Coloumb failure envelop optimisation. Example with (a) positive slope for higher porosities (34%) and (b) negative (not acceptable) slope for lower porosities (27%).

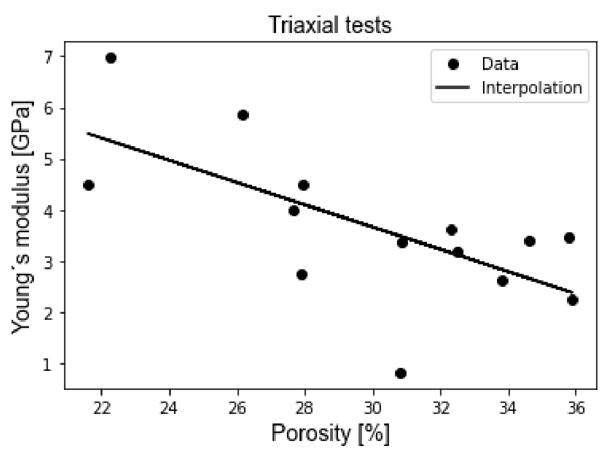

Figure 2.2.3.3: Young's modulus plotted against the porosity of the tested samples. The data is calculated from the results of the single stage triaxial tests.

4.5 Thick Wall Cylinder tests

4.5.1 Test procedure

The Thick Wall Cylinder (TWC) experiments were performed in the FracTech Laboratories (FTL), an independent laboratory in Woking (UK), with twenty-five years of experience working on rock mechanics tests. The samples used for the tests were casted using carbonate rock samples that were extracted from a depth of approximately 1,400 m. The TWC samples were casted into hollowed cylinders, with a length of about 75 mm, an outer diameter of approximately 95 mm and an inner diameter of about 19 mm. The samples were saturated with the brine composition in Table 2.3.1.1.

Table 2.3.1.1: Brine composition.

Strontium (mg/l)	66.24
Na (mg/l)	8996.5
Ca (mg/l)	233.3
Mg (mg/l)	47.8
Ba (mg/l)	0
Fe (mg/l)	0
K (mg/l)	816.4
Cl (mg/l)	13812.8
SO4 (mg/l)	1275.6
HCO3 (mg/l)	1363

The sample was placed between two loading plates. This allowed to apply both an axial load and an axial fluid flow through the borehole of the tested sample. The specimen was also radially enclosed in a mesh and a load cell to apply a radial load and a radial fluid flow. Radial flow was applied by means of a centrifugal pump so that a prescribed value of fluid pressure could be kept constant at the outer boundary of the sample. A hole in the bottom loading plate allowed to maintain the pressure in the specimen borehole equal to atmospheric pressure and to collect the fluid and the solid fragments produced during the experiment. The onset of solid production was detected by measuring the sudden displacement of a sieve caused by the contact with rock fragments being transported away from the tested sample in the outlet flow. The flows of the outlet fluid were collected and then filtered to determine the mass of the rock fragments that were produced during the different phases of the experiment. The experiment was conducted as follows:

a) Radial fluid flow was applied to maintain the prescribed fluid pressure at the cylinder boundaries throughout the experiment.

b) The axial and radial loads were ramped hydrostatically until the onset of solid production was detected.

c) The axial and radial load were maintained constant until the end of solid production, and the outlet flow was collected in a tank and then filtered to compute the mass of solid produced in that stage.

d) The axial flow is used to remove potentially remaining rock fragments that were not transported away from the wall of the well with the radial flow. The outlet flow was collected in a tank and then filtered to compute the mass of solid produced in that stage.

e) The axial and radial loads were ramped hydrostatically until the confinement was increased by 10% of the confinement in the previous step.

f) Steps (c), (d), and (e) were repeated until the specimen showed signs of total collapse.

4.5.2 Sample description

The ATW test procedure described above was performed on 6 samples in total. The geometry and properties of each tested sample are shown in Table 2.3.2.1. All samples were analysed with X-ray CT scans before and after the test. Due to the high degree of heterogeneity, all samples have different porosity, ranging from 16% for the weaker samples to 35% for the more competent samples. X-ray CT scans of the six samples before testing are shown in Figure 2.3.2.1.

Table 2.3.2.1: Geometry and properties of the tested TWC samples.

Well:	Sample No:	Core Depth (ft):	Porosity (%)	Differential Pressure (psi)	Flow Rate (ml/min)	Onset of Sand (psi)	Failure Stress (psi)
F6-2	5	4551.50	31.2		160/216/267	1109	1470
F6-2	1	4426.90	29.9	12	340-20	665	1430
F6-2	6	4572.90	31.6	17	340-72	1212	1402
F6-2	3	4491.20	25.2	130	110-13	1584	4091
F6-2	2	4441.8	22.1				
F6-2	4	4525.1	20.3				
F6-2	7	4654.9	18.2				

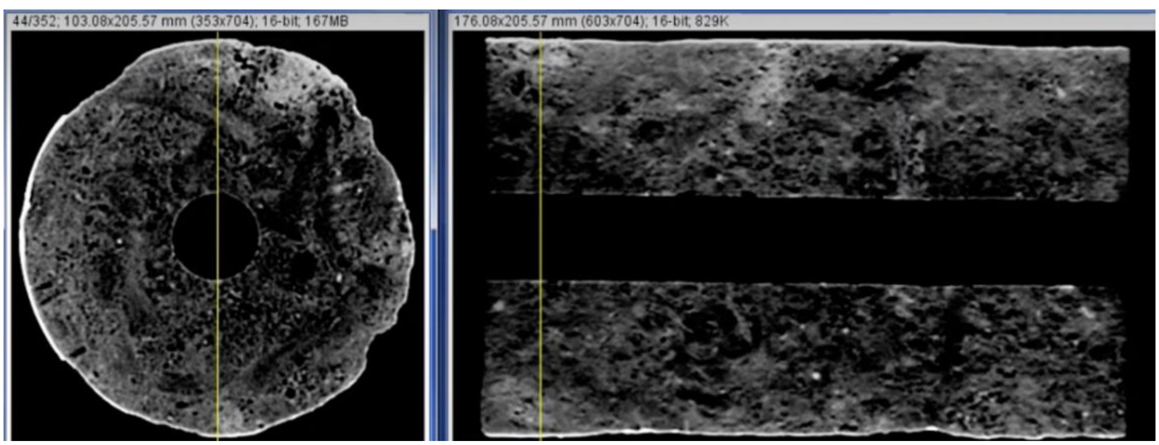

Figure 2.3.2.1: X-ray CT scans of the sample before testing.

Due to the difference in strengths and permeabilities of the testes samples, different values of radial flow rates and consequently fluid pressure at the cylinder boundaries were prescribed in each test, as shown in Table 2.3.2.1.

Table 2.3.2.1: TWC test conditions for each experiment.

Well:	Sample No:	Core Depth (ft):	Porosity (%)	Differential Pressure (psi)	Flow Rate (ml/min)	Onset of Sand (psi)	Failure Stress (psi)
F6-2	5	4551.50	31.2		160/216/267	1109	1470
F6-2	1	4426.90	29.9	12	340-20	665	1430
F6-2	6	4572.90	31.6	17	340-72	1212	1402
F6-2	3	4491.20	25.2	130	110-13	1584	4091
F6-2	2	4441.8	22.1				
F6-2	4	4525.1	20.3				
F6-2	7	4654.9	18.2				

4.5.3 Results

The applied hydrostatic confinement and consequent solid production curves are shown in Figure 2.3.3.1.

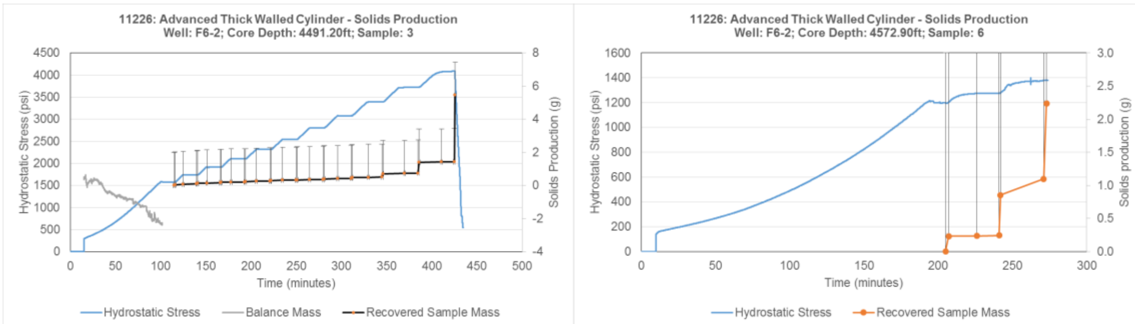

Figure 2.3.3.1: Hydrostatic confinement and consequent solid production curves for the TWC tests.

The X-ray CT scans of the samples before testing are shown in Figure 2.3.3.2. Figure 2.3.3.3 shows the photographs of the inside of the boreholes of specimens after testing.

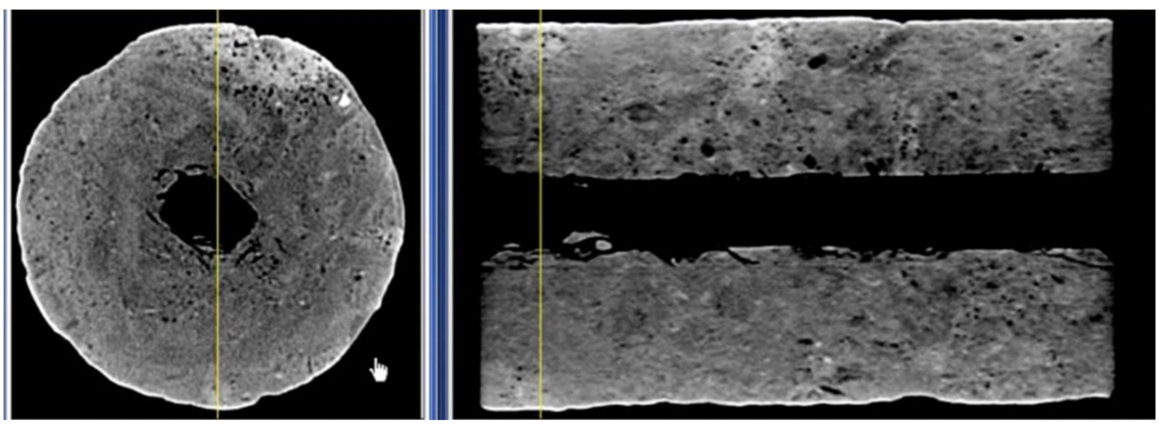

Figure 2.3.3.2: X-ray CT scans of the sample after testing.

Figure 2.3.3.3: Photographs of the inside of the boreholes of specimens after testing (Test 3).

The cumulative solid production percentage is then calculated for each test by dividing the cumulative solid production (g) by the dry mass of the corresponding sample before testing listed in Table 2.3.2.1. Figure 2.3.3.4 shows the cumulative solid production as a percentage of the total mass of the sample against the applied confinement.

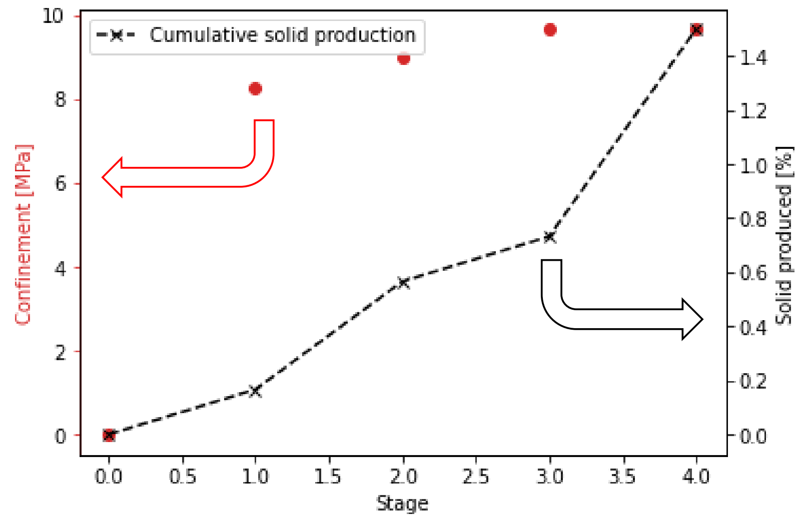

Figure 2.3.3.4: Cumulative solid production in percentage of the total mass of the sample against the applied confinement (Test 3).

4.6 Conclusions

Mechanical tests were conducted to characterise and test the ATWC samples of carbonate rocks with different degrees of porosities. More experiments will be conducted soon, to better permit a correlation between the porosity and mechanical properties of carbonate rock samples. The rest of the TWC tests will also be conducted shortly.

5 Numerical estimations of borehole enlargement and solid production validation

5.1 Introduction

This chapter contains the preliminary validation of the FDEM workflow for the estimation of solid production onset and rate.

5.2 Numerical workflow

A MATLAB/Octave code is used to define the geometry, material properties, boundary conditions and to generate the mesh and the input files that are needed to run the FDEM simulations. The input files are then processed with the FDEM code in the Imperial College High Performance Computing (HPC) facility. This allows us to run many FDEM simulations in parallel. The output files from the simulations are then analysed with a post processing tool (ParaView) and some MATLAB/Octave scripts. Below is an example of the simulation workflow.

5.2.1 Geometry and mesh

First the geometry is defined in the MATLAB code with circular borehole of diameter 19 mm (d) in a disc of outer diameter 95 mm (D), as shown in Figure 3.2.1.1.

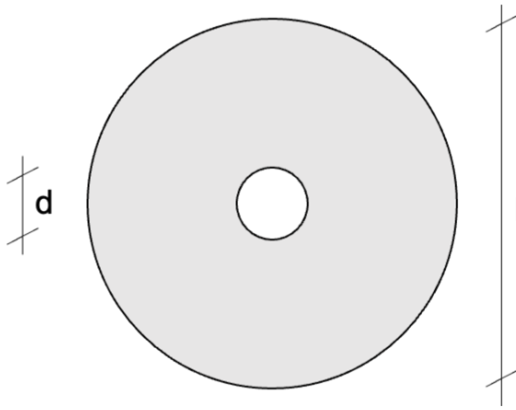

Figure 3.2.1.1: Geometry of the simulated TWC specimen.

The MATLAB code is then provided with the mesh discretisation parameters that are needed to generate the FDEM computational mesh. An unstructured 1.5 mm mesh is used to discretise the simulated domain, as shown in Figure 3.2.1.2.

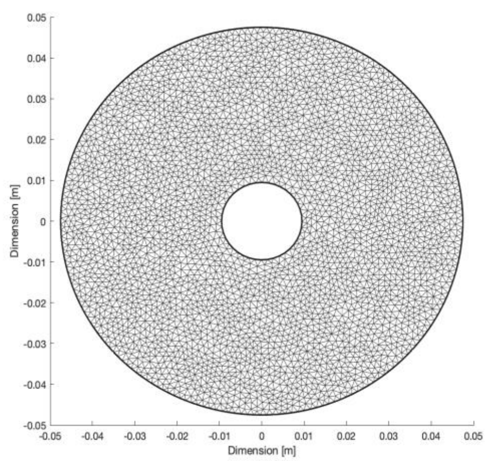

Figure 3.2.1.2: Numerical mesh discretisation of the simulated TWC sample.

5.2.2 Boundary conditions

Consequently, test conditions are defined in the MATLAB code. Confining stress is increased to the prescribed value σ_c and then kept constant. The boundary pore pressure is also increased to the prescribed value of P_b and is kept constant. Figure 3.2.2.1 shows the boundary conditions for the simulation of the TWC test and the profile of the applied pore fluid pressure that goes from the prescribed value P_b on the boundaries of the disc to zero at the inner walls. The logarithmic shape of the fluid pore pressure profile is given by the Thiem equation that was obtained in the previous sections.

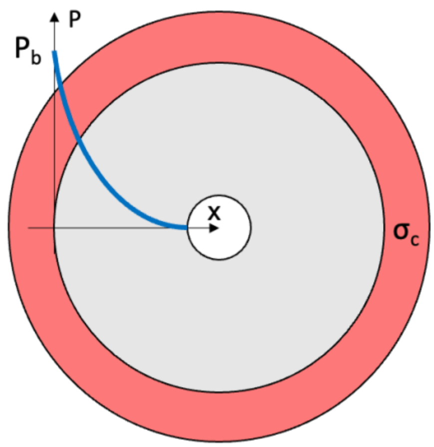

Figure 3.2.2.1: Boundary condition in the FDEM mode.

5.2.3 Numerical parameters

The sample-specific rock properties are also defined in the MATLAB code. The following properties that were previously obtained from mechanical testing on carbonate rock samples have been assigned (see Figure 3.2.3.1): Density [kg/m^3], Young's modulus [GPa]; Poisson's ratio [/]; Tensile strength [MPa]; Energy release rate (Mode I) [J/m^2]; Internal cohesion [MPa]; Internal friction coefficient [/]; Energy release rate (Mode II) [J/m^2]; Penalty term (Normal) [N/m]; Penalty term (Tangential) [N/m]. The other numerical parameters (e.g. the time step size and the buffer size for the contact interaction) that are needed in FDEM are then calculated by the MATLAB code and the input files are automatically sent to the HPC facility and allocated in a queue for execution. The results can then be accessed remotely and visualised. The numerical parameters that were used in the simulations are reported in Table 3.2.3.1.

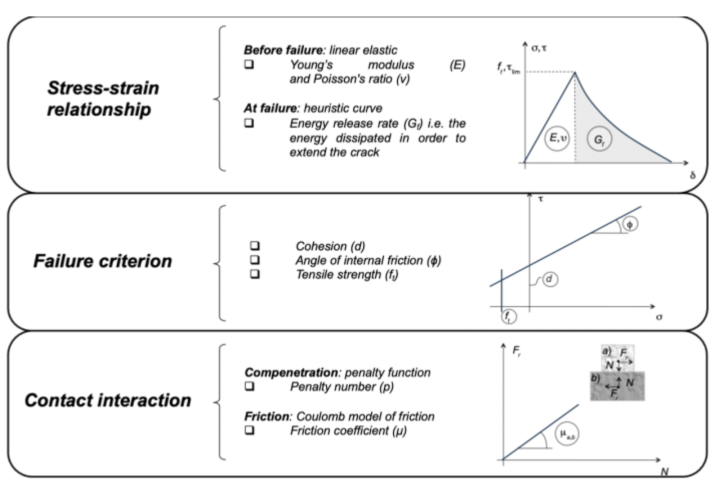

Figure 3.2.3.1: Mechanical parameters in the FDEM mode.

Table 3.2.3.1: Mechanical parameters used in the simulations.

	Simulation Number					
	1	2	3	4	5	6
Density [kg / m^3]			2580			
Young's modulus [GPa]			4.7			
Poisson's ratio [/]			0.26			
Tensile strength [Mpa]			0.81			
Energy release rate (Mode I) [J/m^2]			10			
Internal cohesion [MPa]			3.5			
Internal friction coefficient [/]			0.39			
Energy release rate (Mode II) [J/m^2]			30			
Penalty term (Normal) [N/m]			2.35E+11			
Penalty term (Tangential) [N/m]			2.35E+12			

5.2.4 Element removal and solid production computation

To represent the effect of the fluid flow that transports the rock fragments away from the sample borehole with the outlet flow, the elements in the numerical simulation that reach the area represented by the diagonal shading lines in Figure 3.2.4.1 are removed from the simulation. Figure 3.2.4.2 shows an example of the lapse of the rock elements (in grey) being removed from the simulation when they reach the horizon of the element removal area. The removed elements are shown as white triangles with black edges. The cumulative area of the removed element is then calculated and divided by the total area of the intact sample to compute the percentage of cumulative solid produced at each step of the simulation.

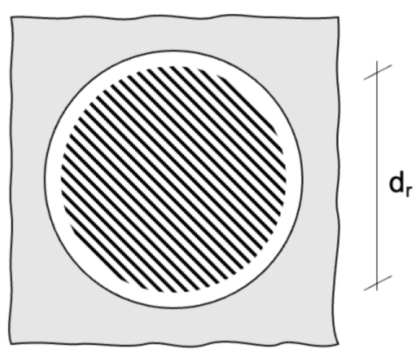

Figure 3.2.4.1: Representation of the element removal area of diameter d_r in the centre of the specimen borehole.

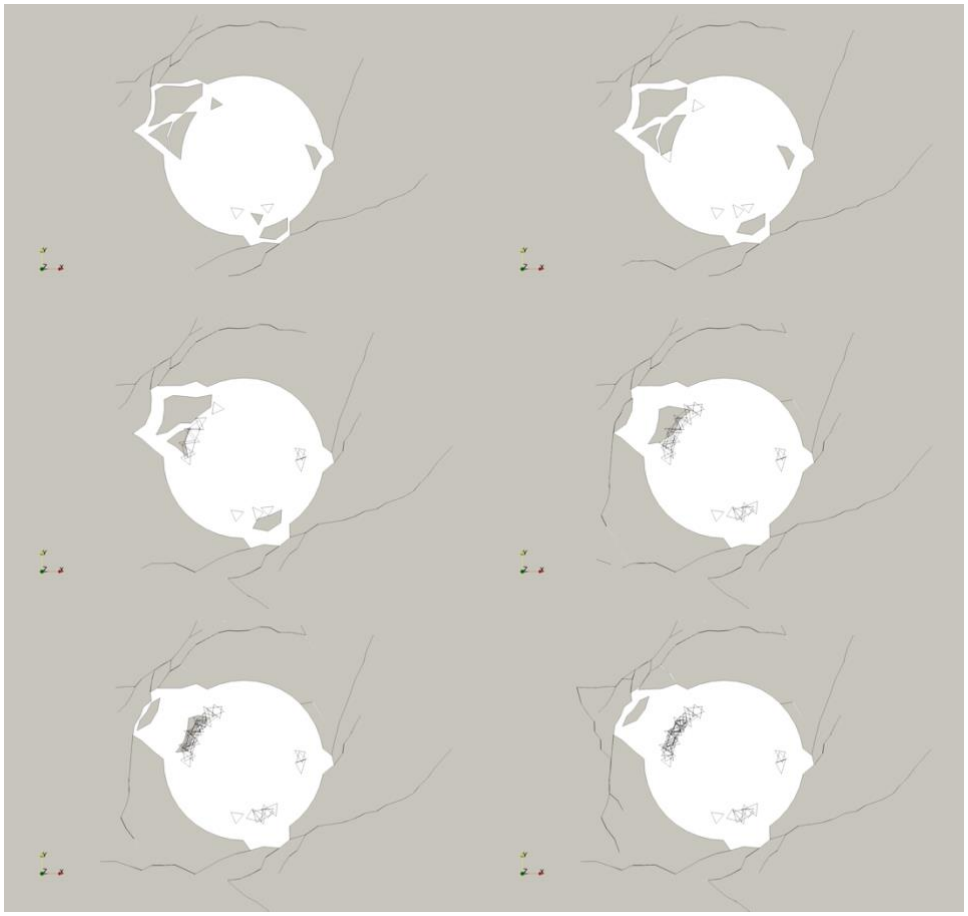

Figure 3.2.4.2: Time lapse of the rock elements (in grey) being removed from the simulation when reaching the horizon of the element removal area. The removed elements are shown as white triangles with black edges.

5.3 Verification

The six TWC tests conducted in FTL will be simulated with the numerical methodology described in the previous sections. The numerical parameters that were used in the simulations to represent the specific rock properties of each TWC sample are reported in Table 3.2.3.1. The different confinements and boundary pore fluid pressures applied in each simulation are reported in Table 3.3.1. Figure 3.3.1 shows the simulation results for a hydrostatic pressure of 6 MPa and a boundary pore pressure of 0.12 MPa in terms of (a) pore pressure, (b) first principal stress, (c) second principal stress fields.

Table 3.3.1: Boundary conditions in the simulations: confinements and boundary pore fluid pressures applied in each simulation.

	Simulation Number					
	1	2	3	4	5	6
Boundary pore fluid pressure [Mpa]			0.12			
Max confining pressure [MPa]			11.5			

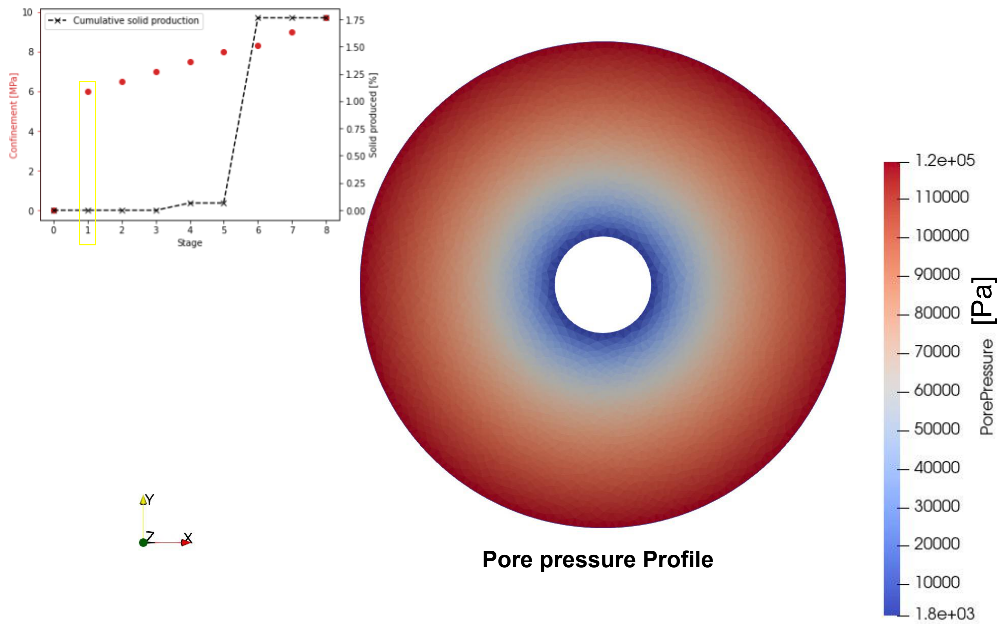
Cumulative solid production
Confinement [MPa]
Solid produced [%]
Stage
Pore pressure Profile
PorePressure [Pa]
1.2e+05
110000
100000
90000
80000
70000
60000
50000
40000
30000
20000
10000
1.8e+03

(a)

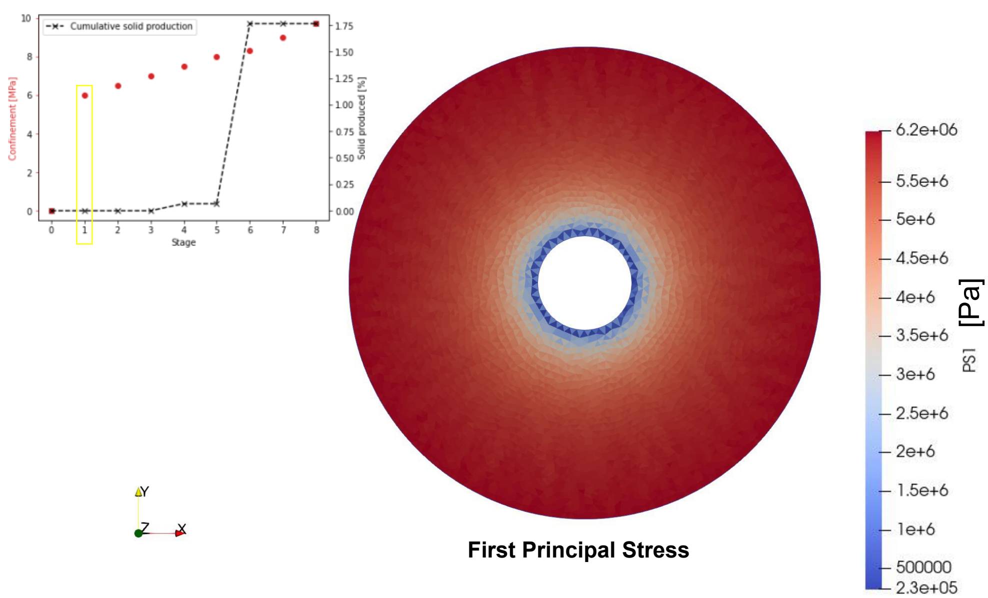
Cumulative solid production
Confinement [MPa]
Solid produced [%]
Stage
First Principal Stress
PS1 [Pa]
6.2e+06
5.5e+6
5e+6
4.5e+6
4e+6
3.5e+6
3e+6
2.5e+6
2e+6
1.5e+6
1e+6
500000
2.3e+05

(b)

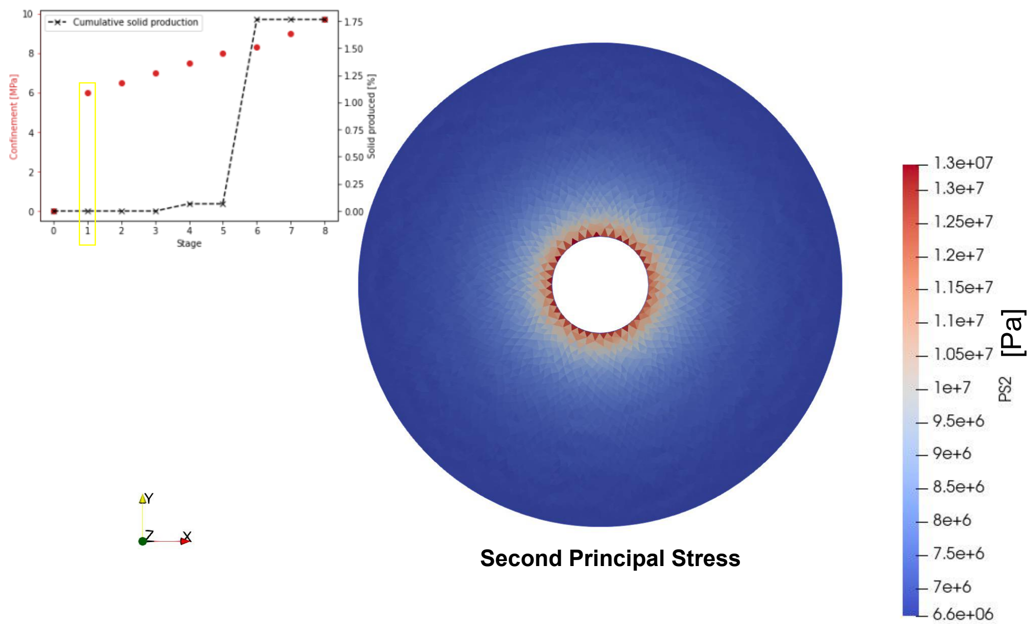

(c)

Figure 3.3.1: Simulation results for a hydrostatic pressure of 6 MPa and a boundary pore pressure of 0.12 MPa: (a) pore pressure, (b) first principal stress, (c) second principal stress fields.

Figure 3.3.2 shows the simulation results for a boundary pore pressure of 0.12 MPa and different levels of hydrostatic pressure confinements: (a) 6 MPa, (b) 7.5 MPa, (c) 8 MPa, (d) 8.3 MPa, (e) 9 MPa, and (f) 9.7 MPa. With the increase in hydrostatic confinement, the breakouts and the extent of the fractures are also increasing. During this process, rock fragments are produced and dislodged toward the centre of the borehole.

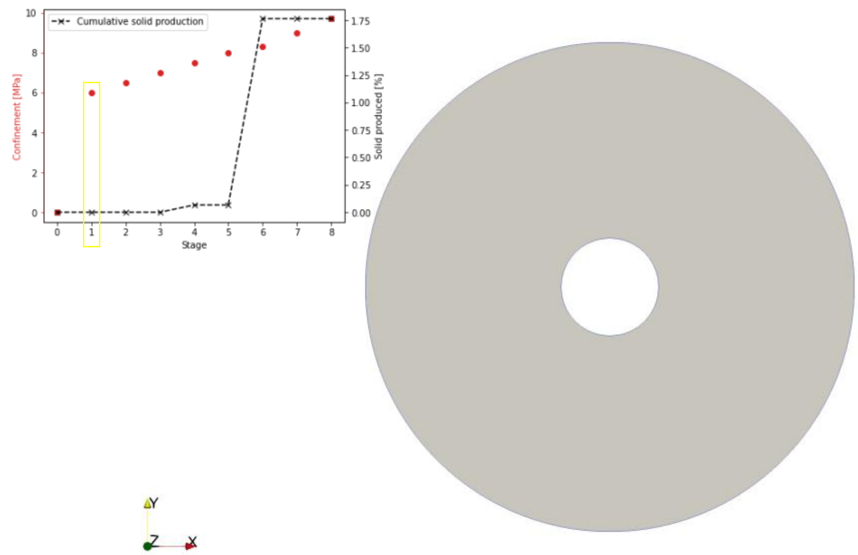
Cumulative solid production
Confinement [MPa]
Solid produced [%]
Stage
Y
Z
X

(a)

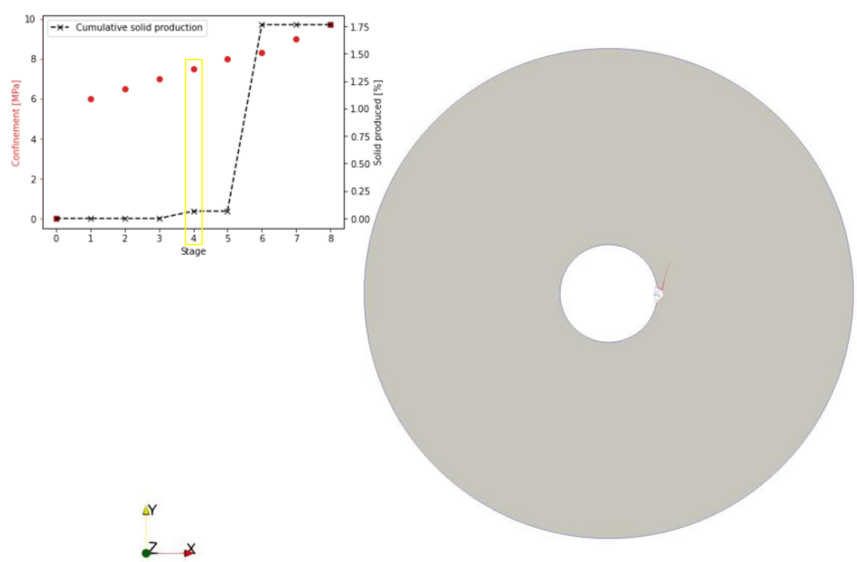
Cumulative solid production
Confinement [MPa]
Solid produced [%]
Stage
Y
Z
X

(b)

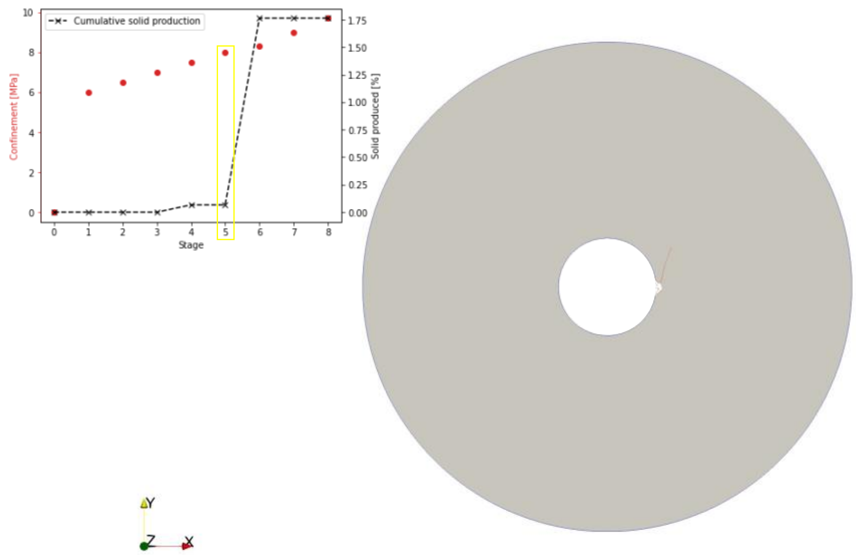

Cumulative solid production
Confinement [MPa]
Solid produced [%]
Stage
Y
Z
X

(c)

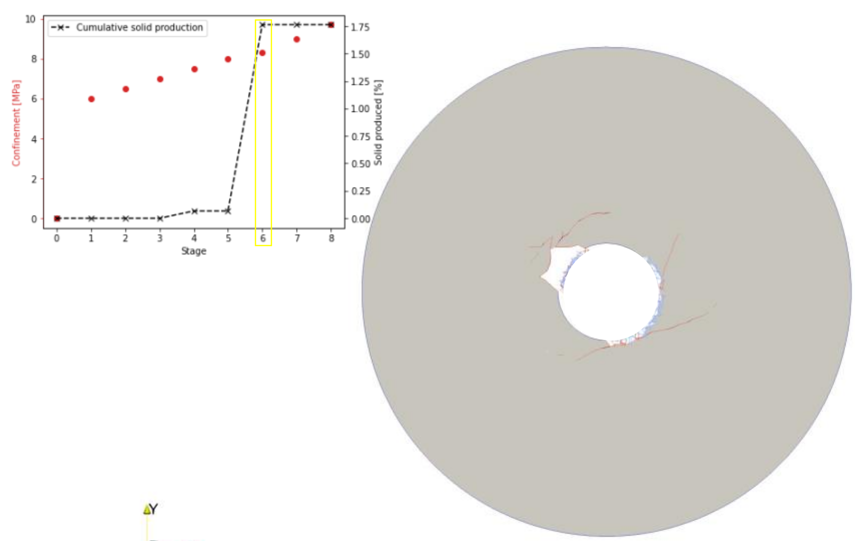

Cumulative solid production
Confinement [MPa]
Solid produced [%]
Stage
Y
Z
X

(d)

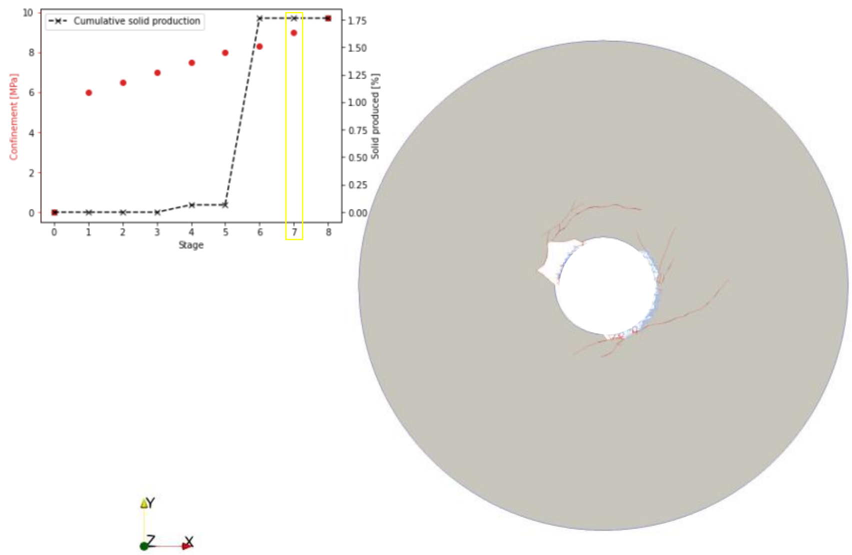

(e)

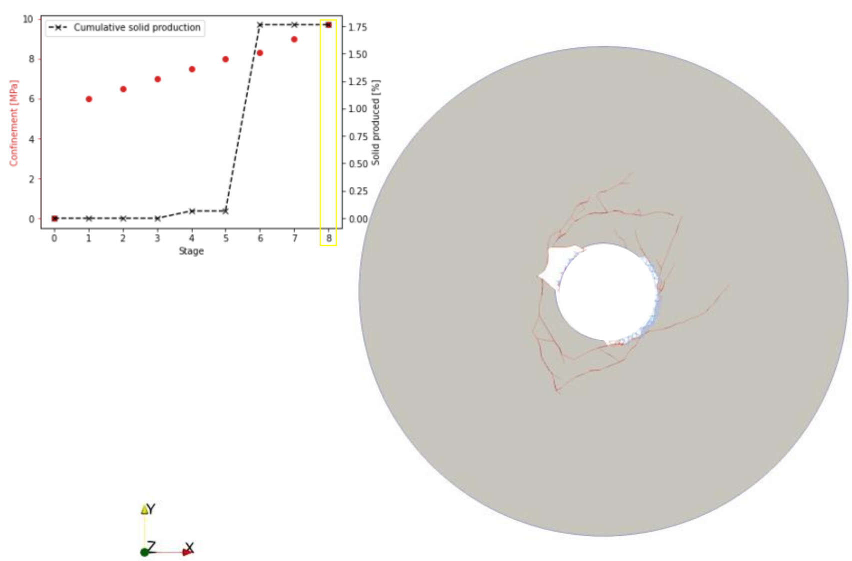

(f)

Figure 3.3.2: Simulation results for a boundary pore pressure of 0.12 MPa and different levels of hydrostatic pressure confinement: (a) 6 MPa, (b) 7.5 MPa, (c) 8 MPa, (d) 8.3 MPa, (e) 9 MPa, and (f) 9.7 MPa.

A comparison between the percentage of solid produced in two experiments (blue and orange dots) and in the preliminary FDEM simulation (black dashed line) is shown in Figure 3.3.3. These preliminary results show a similar onset and rate of solid production for the target experiment (experiment number 3, that has the same boundary pore pressure of the FDEM simulation).

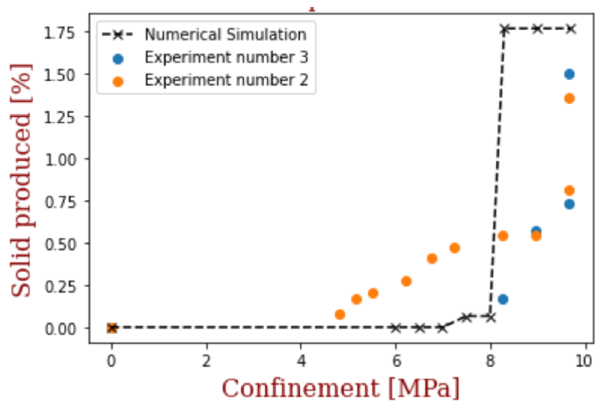

Figure 3.3.3: Comparison between the percentage of solid produced in two experiments (blue and orange dots) and in the preliminary FDEM simulation (black dashed line).

5.4 Conclusions

Novel Thick-Walled-Cylinder (TWC) tests and other rock mechanical characterisation tests are being conducted in the FracTech laboratories. The TWC tests involve stresses applied at the outer boundary, as well as radial fluid flow into the borehole. The mass of solids produced during the test is measured in real time.

The TWC tests are being modelled using combined Finite-Discrete Element (FDEM) simulations, which include the poroelastic effects caused by the flow of pore fluid. The stresses and displacements predicted by this new coupled code have been validated against those computed by Firedrake. (Note that this latter code is not capable of modelling rock damage and solids production). As the mechanical properties of the tested TWC samples are not yet available for model calibration, the model parameters used in the simulations are based on mechanical properties that were obtained from previous characterisations of carbonate rock samples ("Batch 1").

The preliminary results obtained with the FDEM code show reasonably good agreement, both in terms of onset of solids production and cumulative solids produced, with Experiment Number 3 that was conducted in the FracTech Laboratories. Additional lab tests and simulations are ongoing.

6 Simulation of well conditions

6.1 Workflow and input data

A MATLAB/Octave code is used to define the geometry, material properties, boundary conditions and to generate the mesh and the input files that are needed to run the FDEM simulations. The input files are then processed with the FDEM code in the Imperial College High Performance Computing (HPC) facility. This allows us to run a large number of FDEM simulations in parallel. The output files from the simulations are then analysed with a post processing tool (Paraview) and some MATLAB/Octave scripts. Below is an example of the simulation workflow.

First the geometry is defined in the MATLAB code. A circular borehole of diameter 20 cm in a square domain of edge that is forty times the borehole diameter, as shown in Fig. 17.

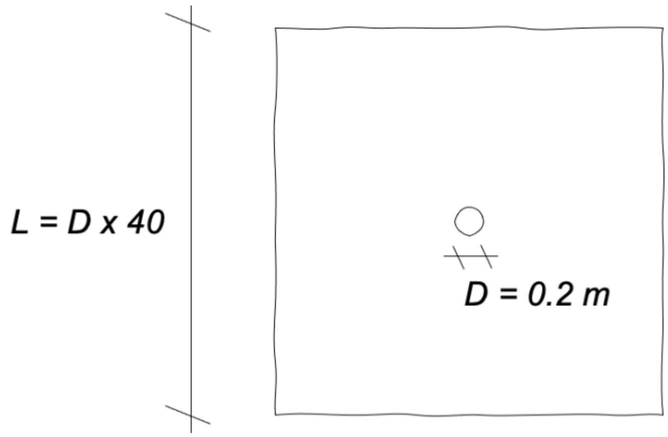

Figure 17: Geometry of the simulated reservoir

Consequently, the reservoir specific rock properties and *in-situ* conditions are also defined in the MATLAB code (as summarised in Fig. 18). The following properties that were previously obtained from mechanical testing on sandstone have been assigned: Density = 2,000 kg / m^3 ; Young's modulus = 19.5 GPa ; Poisson's ratio = 0.265 ; Tensile strength = 3.5 MPa ; Energy release rate (I) = 30 J/m^2 ; UCS = 53.15 MPa ; Internal cohesion = 17.9 MPa ; Internal friction angle = 22° ; Energy release rate (II) = 190 J/m^2 . The in-situ stresses are σ_x = 12.76 MPa and σ_y = 25.51 MPa. In this example there is no pore pressure, making the applied stresses equal to effective stresses. The mechanical parameters that have been used for this simulation are not representative of reservoir F6, as this simulation was run *before* the document named "Data Rock Mechanics" containing that set of parameters was sent to the IC team (on September 10th).

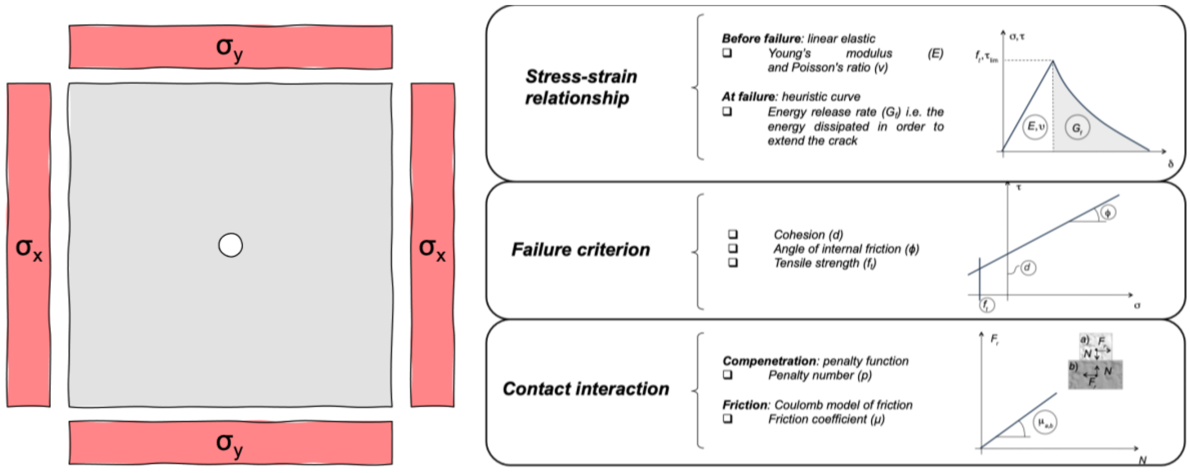

Figure 18: Boundary conditions and mechanical parameters in the FDEM mode

The MATLAB code is then provided with the mesh discretisation parameters that are needed to generate the FDEM computational mesh. In this case the triangular mesh elements in the vicinity of the borehole have a size of $D \times 0.025$ (where higher accuracy is needed) and the mesh on the outer boundaries have a size $D \times 20$. The mesh discretisation of the simulated domain is shown in Fig. 19.

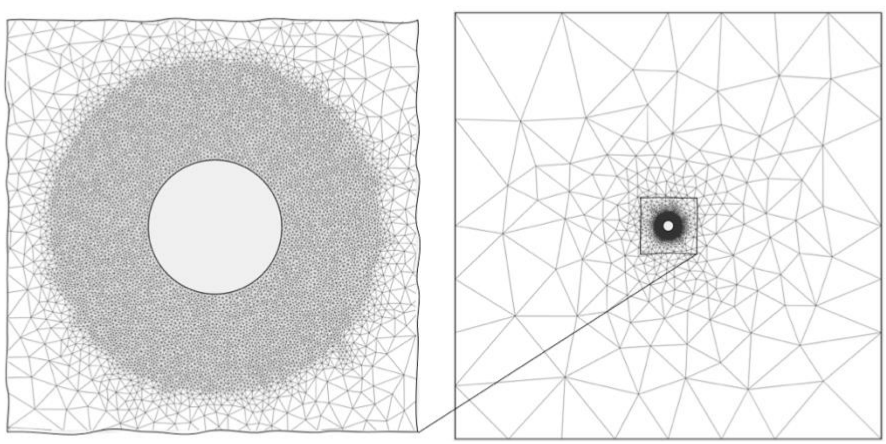

Figure 19: Numerical mesh discretisation of the simulated domain

The other numerical parameters (e.g. the time step size and the buffer size for the contact interaction) that are needed in FDEM are then calculated by the MATLAB code and the input files are automatically sent to the HPC facility and allocated in a queue for execution. The results can then be accessed remotely and visualised. A frame from the output files for this simulation is shown in Fig. 20. The results show the maximum principal stress field (reported here as σ_{III}) and the fracture mode during the progressive failure of the borehole walls and the production of rock fragments.

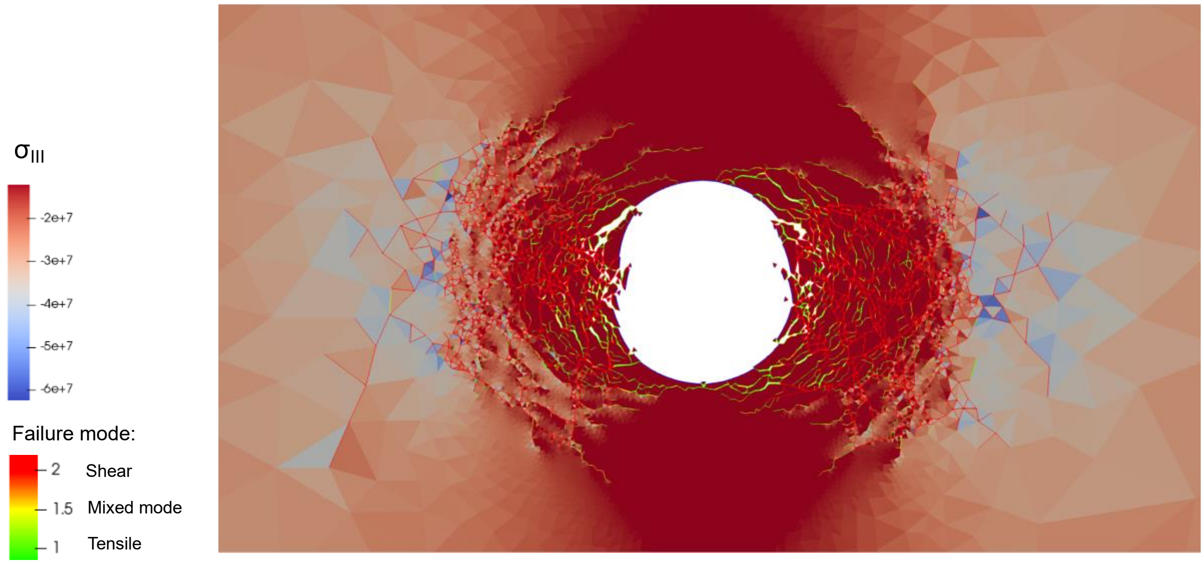

Figure 20: Output from the FDEM numerical simulation showing the third principal stress field and the fracture mode during the fragmentation of the borehole walls

The simulations that have been presented in this section have been obtained using the 2D version of the FDEM code. This has been done to simplify the computational model and reduce the run time in this first phase of the research project. We intend to transition to 3D FDEM simulations in a later stage of the project.

The mechanical tests data will be used to calibrate the input parameters that are needed in the FDEM numerical simulations. Triaxial test results will be used to define the Young's modulus, Poisson ratio, cohesion and internal friction angle. Results from Brazilian disc tests will provide the tensile strength parameter in input in the simulation. Alternatively, if Brazilian tests results are not available, correlations with the parameters obtained from triaxial tests might be used to define an estimate for the tensile strength of the simulated carbonate rocks. The remaining parameters that are needed in for FDEM simulations (e.g. Mode I and II energy release rates) can be then optimised by simulating the triaxial tests with FDEM and selecting the optimal combination of parameters that allows a match between the simulated and experimental stress-strain curves.

The water weaking effects on the solid production in a carbonate reservoir of interest can be investigated in the next phases of this research after that a sufficient amount of experimental data (e.g. triaxial tests) on carbonate rocks with different water contents have been collected. The following methodology can be used:

1. To develop an analytical relationship between the degree of saturation (i.e. water content) of the carbonate under consideration and its mechanical properties;

2. To run a FDEM simulation of borehole under in-situ stress conditions and 0% saturation until equilibrium;
3. To ramp down the mechanical properties of the carbonate affected by weakening until the degree of saturation under study is met. Wait until equilibrium is reached;
4. To record the area of fragmented carbonates from (3) and infer a measure of solid production for that particular borehole geometry, mechanical properties and degree of saturation.

6.2 Results

6.3 Conclusions

7 Tool for the prediction of solid production

7.1 Example

7.2 Conclusions

8 Conclusions

References

AL-Aamri, M., Mahajan, S., Sujith, N., Waleed, B., & Marta, B. R. (2020). Practical Approach for Solid Production Prediction and Completion Strategy Decisions in Horizontal Wells – A Case study from Cretaceous Carbonate Reservoir – North Oman. In *International Petroleum Technology Conference* (p. 14). International Petroleum Technology Conference. https://doi.org/10.2523/IPTC-20130-Abstract

Applied Modelling and Computation Group (AMCG) at Imperial College London. (2018). *www.solidityproject.com*. www.solidityproject.com

Asadi, M. S., Khaksar, A., Hughes, B., Nguyen, H. Q., & Manapov, T. F. (2017). Solids production prediction and management in a high porosity carbonate reservoir-a case study from offshore Vietnam. *Society of Petroleum Engineers - SPE/IATMI Asia Pacific Oil and Gas Conference and Exhibition 2017*, *2017-Janua*.

Asadi, M. S., Khaksar, A., Ring, M. J., Saric, D., & Yin Yin, M. (2016). Solids production prediction and management for oil producers in highly depleted reservoirs in a mature Malaysian field. *Proceedings - SPE Annual Technical Conference and Exhibition*, *2016-Janua*. https://doi.org/10.2118/181583-ms

Cuss, R. J., Rutter, E. H., & Holloway, R. F. (2003). Experimental observations of the mechanics of borehole failure in porous sandstone. *International Journal of Rock Mechanics and Mining Sciences*, *40*(5), 747–761. https://doi.org/10.1016/S1365-1609(03)00068-6

Duan, K., & Kwok, C. Y. (2016). Evolution of stress-induced borehole breakout in inherently anisotropic rock: Insights from discrete element modeling. *Journal of Geophysical Research: Solid Earth*, *121*(4), 2361–2381. https://doi.org/10.1002/2015JB012676

Evans, R. H., & Marathe, M. S. (1968). Microcracking and stress-strain curves for concrete in tension. *Matériaux et Constructions*, *1*(1), 61–64. https://doi.org/10.1007/BF02479001

Farsi, A., Bedi, A., Latham, J. P., & Bowers, K. (2020). Simulation of fracture propagation in fibre-reinforced concrete using FDEM: an application to tunnel linings. *Computational Particle Mechanics*, *7*(5), 961–974. https://doi.org/10.1007/s40571-019-00305-5

Farsi, A., Xiang, J., Latham, J.-P., Carlsson, M., Stitt, E. H., & Marigo, M. (2020). Packing simulations of complex-shaped rigid particles using FDEM: An application to catalyst pellets (under review). *Powder Technology*.

Ghassemi, A., & Pak, A. (2015). Numerical simulation of sand production experiment using a coupled Lattice Boltzmann-Discrete Element Method. *Journal of Petroleum Science and Engineering*, *135*, 218–231. https://doi.org/10.1016/j.petrol.2015.09.019

Khaksar, A., Rahman, K., Ghani, J., & Mangor, H. (2008). Integrated geomechanical study for hole stability, sanding potential and completion selection: A case study from South East Asia. *Proceedings - SPE Annual Technical Conference and Exhibition*, *4*, 2551–2567. https://doi.org/10.2118/115915-ms

King, R. C., Tingay, M. R. P., Hillis, R. R., Morley, C. K., & Clark, J. (2010). Present-day stress orientations and tectonic provinces of the NW Borneo collisional margin. *Journal of Geophysical Research: Solid Earth*, *115*(10), 1–15. https://doi.org/10.1029/2009JB006997

Li, Y., Qu, Y., He, Q., & Tang, C. (2020). Mesoscale numerical study on the evolution of borehole breakout in heterogeneous rocks. *International Journal for Numerical and Analytical Methods in Geomechanics*, *44*(8), 1219–1236. https://doi.org/10.1002/nag.3058

Ma, X., & Haimson, B. C. (2016). Failure characteristics of two porous sandstones subjected to true triaxial stresses. *Journal of Geophysical Research: Solid Earth*, *121*(9), 6477–6498. https://doi.org/10.1002/2016JB012979

Meier, T., Rybacki, E., Reinicke, A., & Dresen, G. (2013). Influence of borehole diameter on the formation of borehole breakouts in black shale. *International Journal of Rock Mechanics and Mining Sciences*, *62*, 74–85. https://doi.org/10.1016/j.ijrmms.2013.03.012

Mohamad-Hussein, A., & Ni, Q. (2018). Numerical modeling of onset and rate of sand production in perforated wells. *Journal of Petroleum Exploration and Production Technology*, *8*(4), 1255–1271. https://doi.org/10.1007/s13202-018-0443-6

Munjiza, A. (2004). *The Combined Finite-Discrete Element Method*. Wiley.

Munjiza, A., Andrews, K. R. F., & White, J. K. (1999). Combined single and smeared crack model in combined finite-discrete element analysis. *International Journal for Numerical Methods in Engineering*, *44*(1), 41–57. https://doi.org/10.1002/(SICI)1097-0207(19990110)44:1<41::AID-NME487>3.0.CO;2-A

Munjiza, A., Xiang, J., Garcia, X., Latham, J. P., D'Albano, G. G. S., & John, N. W. M. (2010). The Virtual Geoscience Workbench, VGW: Open Source tools for discontinuous systems. *Particuology*, *8*(2), 100–105. https://doi.org/10.1016/j.partic.2009.04.008

Nurhandoko, B. E. B., & Listyobudi, M. (2018). *Thick Walled Core Testing for Sanding Analysis of Chalky Carbonate Reservoir in Production Borehole*. *September*, 24–27.

Papamichos, E. (2020). Analytical models for onset of sand production under isotropic and anisotropic stresses in laboratory tests. *Geomechanics for Energy and the Environment*, *21*, 100149. https://doi.org/10.1016/j.gete.2019.100149

Papamichos, E., Berntsen, A. N., Cerasi, P., Vandycke, S., Baele, J. M., Fuh, G. F., Han, G., & Kristiansen, T. G. (2012). Solids production in chalk. *46th US Rock Mechanics / Geomechanics Symposium 2012*, *1*, 464–475.

Papamichos, E., & Furui, K. (2019). Analytical models for sand onset under field conditions. *Journal of Petroleum Science and Engineering*, *172*(February 2018), 171–189. https://doi.org/10.1016/j.petrol.2018.09.009

Papamichos, E., Tronvoll, J., Skjærstein, A., & Unander, T. E. (2010). Hole stability of Red Wildmoor sandstone under anisotropic stresses and sand production criterion. *Journal of Petroleum Science and Engineering*, *72*(1–2), 78–92. https://doi.org/10.1016/j.petrol.2010.03.006

Rahmati, H., Jafarpour, M., Azadbakht, S., Nouri, A., Vaziri, H., Chan, D., & Xiao, Y. (2013). Review of Sand Production Prediction Models. *Journal of Petroleum Engineering*, *2013*, 1–16. https://doi.org/10.1155/2013/864981

Rougier, E., Knight, E., Broome, S., Sussman, A., & Munjiza, A. (2014). Validation of a three-dimensional Finite-Discrete Element Method using experimental results of the Split Hopkinson Pressure Bar test. *International Journal of Rock Mechanics and Mining Sciences*, *70*, 101–108. https://doi.org/10.1016/j.ijrmms.2014.03.011

Shen, B., Stephansson, O., & Rinne, M. (2014). *Modelling Rock Fracturing Processes*. Springer Netherlands. https://doi.org/10.1007/978-94-007-6904-5

Song, Y., Ranjith, P. G., & Wu, B. (2020). Development and experimental validation of a computational fluid dynamics-discrete element method sand production model. *Journal of Natural Gas Science and Engineering*, *73*(July 2019), 103052. https://doi.org/10.1016/j.jngse.2019.103052

Tronvoll, J., & Fjær, E. (1994). Experimental study of sand production from perforation cavities. *International Journal of Rock Mechanics and Mining Sciences And*, *31*(5), 393–410. https://doi.org/10.1016/0148-9062(94)90144-9

Veeken, C. A. M., Davies, D. R., Kenter, C. J., & Kooijman, A. P. (1991). Sand production prediction review. Developing an integrated approach. *Proceedings - SPE Annual Technical Conference and Exhibition*, *Pi*(pt 1), 335–346. https://doi.org/10.2523/22792-ms

Wang, T., Huang, H., Zhang, F., & Han, Y. (2020). DEM-continuum mechanics coupled modeling of slot-shaped breakout in high-porosity sandstone. *Tunnelling and Underground Space Technology*, *98*(May 2019), 103348. https://doi.org/10.1016/j.tust.2020.103348

Wu, B., & Tan, P. (2000). Strength for Application in Sanding Prediction. *Pacific Rocks 2000: Rock around the Rim*.

Xiang, J., Munjiza, A., & Latham, J. (2009). Finite strain, finite rotation quadratic tetrahedral element for the combined finite-discrete element method. *International Journal for Numerical Methods in Engineering*, *79*(8), 946–978. https://doi.org/10.1002/nme.2599

Younessi, A., Gui, F., Asadi, S., & Khaksar, A. (2018). Calibration of sand production prediction models at early field life in the absence of field sanding data. *Society of Petroleum Engineers - SPE Asia Pacific Oil and Gas Conference and Exhibition 2018, APOGCE 2018*.

Younessi, A., & Khaksar, A. (2016). A Novel Approach to Evaluate the Risk of Sanding for Optimum Well Completion Design: A Deep-Water Case Study from Southeast Asia. In *SPE Asia Pacific Oil & Gas Conference and Exhibition* (p. 13). Society of Petroleum Engineers. https://doi.org/10.2118/182160-MS

Zoback, M. D. (2007). *Reservoir Geomechanics*. Cambridge University Press. https://doi.org/DOI: 10.1017/CBO9780511586477